Meteorol. Z. (Contrib. Atm. Sci.), Vol. **28**, No. 4, 273–291 (published online September 20, 2019)

Meso-microscale coupling for wind resource assessment using averaged atmospheric stability conditions

Pablo Durán[1,2*], Cathérine Meissner[2], Kendall Rutledge[3], Ricardo Fonseca[4], Javier Martin-Torres[4,6] and Muyiwa S. Adaramola[1]

[1]Norwegian University of Life Sciences, Ås, Norway
[2]WindSim AS, Fjordgaten 15, Tønsberg, Norway
[3]Novia University of Applied Sciences, Vasa, Finland
[4]Luleå University of Technology, Luleå, Sweden
[5]Instituto Andaluz de Ciencias de la Tierra (CSIC-UGR), Granada, Spain
[6]The Pheasant Memorial Laboratory for Geochemistry and Cosmochemistry, Institute for Planetary Materials, Okayama University at Misasa, Tottori 682-0193, Japan

(Manuscript received July 31, 2018; in revised form April 9, 2019; accepted April 30, 2019)

Abstract

A methodology to couple Numerical Weather Prediction (NWP) models with steady-state Computational Fluid Dynamic (CFD) models for wind resource assessment applications is proposed. NWP simulations are averaged according to their atmospheric stability and wind direction. The averaged NWP simulations are used to generate the initial and boundary conditions of the CFD model. The method is applied using one year of Weather Research and Forecasting (WRF) simulations at the Honkajoki wind farm in Finland and validated by Sonic Detection and Ranging (SODAR) measurements at the site. It is shown that coupled simulations reproduce a more realistic shear for heights above 150 m. In terms of estimated energy production, there is not a big difference between coupled and standalone models. Nevertheless, a considerable difference in the horizontal wind speed patterns can be seen between the coupled and non-coupled approaches. The WRF model resolution has only a small influence on the coupled CFD results.

Keywords: Mesoscale microscale coupling, Wind energy resource assessment, Computational Fluid Dynamics (CFD), Physical downscaling, Boundary conditions

1 Coupled Computational Fluid Dynamics models in wind resource assessment

Recent wind energy projects are being increasingly developed in areas with high terrain complexity. In this kind of terrain, Computational Fluid Dynamic (CFD) models have shown much better performance compared to linear models (Hristov et al., 2014), which have been traditionally used by the wind industry. Furthermore, it has been shown that linear models overpredict the horizontal wind speed for terrain slopes higher than 20°, whereas CFD models accurately predict the wind (Yamaguchi et al., 2002). For these reasons, over recent years CFD models have become more preferred for wind resource assessment. Among commercial CFD codes for wind resource assessment, mostly steady-state modelling is available because of its reasonable use of computational power.

The simulated flow of CFD models depend on the prescribed initial and boundary conditions. Typically, these boundary conditions are imposed as analytical logarithmic wind profiles. CFD models that utilize this type of boundary conditions are referred in this work as "standalone". This approach has been traditionally used in the wind industry given their simplicity and relatively good performance when the atmospheric conditions are predominantly neutral. Nevertheless, those theoretical profiles often deviate from the observed wind profile in the area. One way to use profiles that are more realistic is to use atmospheric data calculated by Numerical Weather Prediction (NWP) models. The use of atmospheric conditions derived from an NWP model to feed a local-scale model is referred in the literature as meso-to-microscale modelling.

NWP models can reproduce mesoscale and regional wind circulation phenomena such as baroclinic pressure systems and thermal winds. Therefore, they can provide more realistic boundary conditions for CFD models than simple analytical profiles. The use of NWP model data is very common in the wind industry because of its global coverage for several decades (Al-Yahyai et al., 2010). Nevertheless, even the finest mesoscale NWP models, with horizontal grid resolutions of several hundred of meters, are not sufficient for the correct representation of the orography. This prevents a good microscale wind

*Corresponding author: Pablo Durán, Norwegian University of Life Sciences, Universitetstunet 3, 1430 Ås, Norway, e-mail: paduran@nmbu.no

DOI 10.1127/metz/2019/0937
Gebrüder Borntraeger Science Publishers, Stuttgart, www.borntraeger-cramer.com

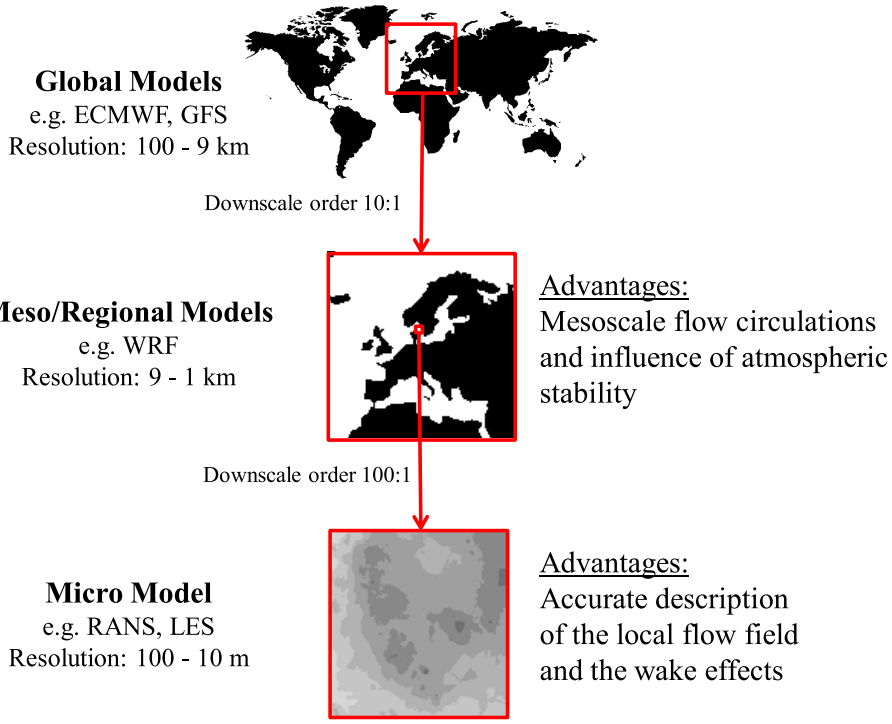

Figure 1: Spatial resolution and advantages of different numerical models used to simulate the wind flow.

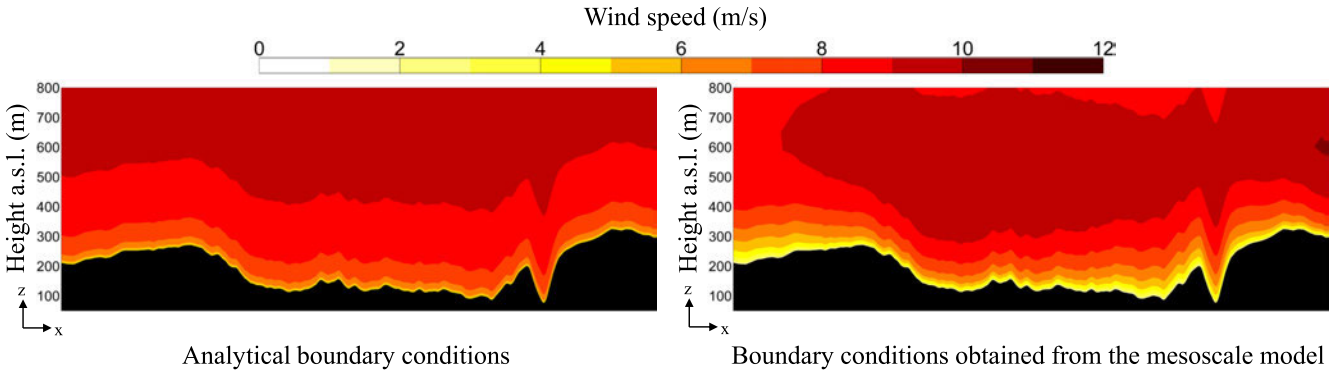

Figure 2: Example of boundary conditions for standalone (left panel) and coupled (right panel) CFD simulations.

resource estimation, especially in complex sites (Bilal et al., 2016a). It is expected that this drawback can be corrected by coupling them with microscale models like RANS CFD models, which have a horizontal grid resolution of tens of meters (Fig. 1). For this reason, the meso-to-microscale models are being widely studied in the industry and literature.

Meso-microscale methodologies that integrate input from an NWP model into a nested CFD model with finer grid are defined as physical downscaling methods (Sanz Rodrigo et al., 2017a). Different physical downscaling methods differ mainly in the downscaling procedure, the mesoscale and microscale model used, and their application (Table 1). The Weather Research and Forecasting (WRF) model (Skamarock et al., 2008) is one of the most commonly used NWP models and therefore it is expected that it is also one of the most commonly used for downscaling purposes. On the other hand, the most used CFD models correspond to large eddy simulation (LES) and Reynolds-averaged Navier–Stokes (RANS) models. Many RANS model codes exist, among which WindSim, OpenFOAM, FLUENT and VENTOS are the most cited in the literature.

In general terms, LES models are more accurate but more computational demanding in comparison with RANS models (Duraisamy, 2014). For this reason, RANS CFD models are more commonly used in the wind energy industry (Duraisamy, 2014; Veiga Rodrigues et al., 2016). In the current study the CFD Software WindSim, which uses steady-state RANS equations, is used.

There are two main approaches for physical downscaling of mesoscale model results using CFD models. One approach is to run the CFD simulation using analytical boundary conditions and scale the 3-D CFD wind field with the mesoscale wind speed at one or several se-

Table 1: Classification of previous studies that use meso-microscale coupling. RANS based models are highlighted in bold.

Model			
Mesoscale	Microscale	Application	Reference(s)
WRF	**WindSim**	Wind energy	Bilal et al., 2016a; Bilal et al., 2016b; Castellani et al., 2006; Meissner et al., 2015
WRF	**OpenFOAM**	Wind energy Urban flow	Boutanios et al., 2010; Leblebici et al., 2014; Leblebici and Tuncer, 2015 Miao et al., 2013; Zheng et al., 2015
WRF	HELIOS	Wind energy	Gopalan et al., 2014; Sitaraman, 2013; Sitaraman et al., 2013
Others	**FLUENT**	Wind energy Urban flow	Li et al., 2010; Schneiderbauer and Pirker, 2010 Li et al., 2007; Solazzo et al., 2006
Others*	**VENTOS**	Wind energy Urban flow	Veiga Rodrigues et al., 2008, 2016 Veiga Rodrigues and Palma, 2014
WRF	LES	Wind energy Urban flow	Liu et al., 2011; Lundquist et al., 2008; Mirocha et al., 2013, 2014; Mirocha and Kirkil, 2010; Moeng et al., 2007; Muñoz-Esparza et al., 2014; Sanz Rodrigo et al., 2017b Kinbara et al., 2010; Liu et al., 2012; Nakayama et al., 2011
MM5	Various CFD	Urban flow	Baik et al., 2009; Nozu et al., 2009; Solazzo et al., 2006; Takemi et al., 2006
Others	Linear	Wind energy	Al-Yahyai et al., 2012; Badger et al., 2014; Carvalho et al., 2013; Murakami et al., 2003; Yu et al., 2006

*Mostly WRF

Table 2: List of publications that conduct meso-microscale physical downscaling with RANS CFD models.

Reference	Downscaling method	Type of simulation	Long term statistics or duration	Application
Li et al., 2007	Direct coupling	Steady-state	Selected NWP time-steps	Urban wind flow
Zheng et al., 2015	Direct coupling	Steady-state	2 days approx.	Urban wind flow
Folch et al., 2016	Scaled Default CFD	Steady-state	24 directional sectors	Gas dispersion
Sanz Rodrigo et al., 2010	Scaled Default CFD	Steady-state	12 directional sectors	Regional wind map
Bilal et al., 2016a	Scaled Default CFD	Steady-state	12 directional sectors	Wind energy production
Duraisamy et al., 2014	Direct coupling	Steady-state	Clustering	Wind energy production

lected grid points. The second approach, referred to as direct coupling in the literature (Sanz Rodrigo et al., 2017a), uses the NWP model output to define the initial and boundary conditions of the CFD simulation (Fig. 2). The scope of this study is to explore the capabilities of the latter approach.

Most of the literature about coupled RANS CFD models is focused on unsteady simulations which allows for the temporal description of wind flow (Baik et al., 2009; Castro et al., 2015; Li et al., 2010; Veiga Rodrigues et al., 2016; Veiga Rodrigues and Palma, 2014; Schneiderbauer and Pirker, 2010). Wind resource assessment models used in the wind industry are usually validated with measurements covering some years, which makes unsteady simulations too expensive in terms of time and computational power. Hence, steady-state simulations are preferred in the wind industry. However, most of the previous studies on coupled steady-state CFD models (see Table 2) have not explored direct coupling for wind energy applications.

In this work, we propose a direct coupling methodology for steady-state CFD simulations for wind resource assessment purposes. It intends to improve the CFD simulations by transferring the average wind speed patterns from the mesoscale model to the CFD model. The consideration of different atmospheric stability conditions in the coupling procedure allows the CFD to capture the observed predominant wind flow conditions, while still making a reasonable use of computational resources in the context of the industry.

This paper is divided into five sections. In Section 2 details about the validation site, datasets, coupled numerical models and validation methodology, are presented. In Section 3 the coupling methodology applied to the WRF and WindSim models is presented. In Section 4 the coupling model is evaluated to then provide conclusions in Section 5.

2 Dataset, models and methods

In the following subsections, the measurement data as well as the data and set-up used to build the WRF and CFD models are presented. Finally, the validation methodology used in this study is explained.

2.1 Validation site and data sets

The Honkajoki wind farm is used as a validation site of the proposed methodology. The wind farm consists of

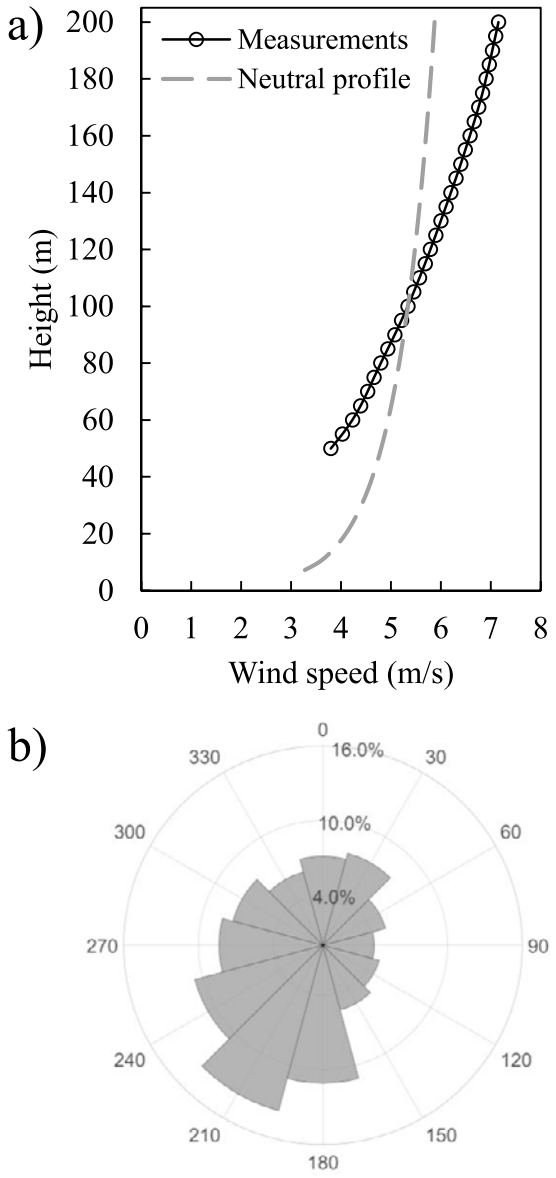

Figure 3: a) Measured vertical profile of mean horizontal wind speed and b) wind rose at 100 meters.

9 Nordex N117/2400 units with a hub height of 120 m and a rotor diameter of 117 m. The site is located in Honkajoki municipality of Satakunta region, in Finland, about 3.5 km to the southeast of the town of Honkajoki and around 45–50 km east from the coast. The terrain at the site is flat, with an absolute height difference of approximately 33 m within the area modelled in the microscale domain. The surface cover consists mainly of forest with presence of an urban area belonging to the Honkajoki town, in the north-west corner of the site.

The wind conditions have been monitored through a SODAR positioned at the coordinates 61.98° N, 22.32° E and elevation 117.1 m, between 19 February 2016 and 19 April 2017. For this period ten-minute averages and standard deviations of horizontal and vertical wind components are available at altitudes between 50 m and 200 m above ground level (a.g.l.) with a vertical resolution of 5 m. The measured vertical profile of mean horizontal wind speed has a higher shear compared to a neutral wind profile as shown in Fig. 3. This is due to a strong influence of stable atmospheric conditions in the site, which are common in mainland Finland. As presented in Fig. 3, the main wind directions are southerly (180°) and south-westerly (210° and 240°).

2.2 WRF model

In this study WRF version 3.7.1 is forced with the National Centers for Environmental Prediction Climate Forecast System Reanalysis (CFSR) 6-hourly data (Saha et al., 2010) and is run for 1 year from March 2016 to March 2017. The WRF version used in this work contains most of the improvements made in Polar WRF (Hines and Bromwich, 2008), a modified version of the model optimized for the polar regions and is therefore suitable for this year-long simulation. The wind farm parameterization scheme available in WRF based on Fitch et al. (2012) is switched on in all model domains and set up for the Honkajoki wind farm using turbine data provided by the manufacturer. This scheme assumes that the wind turbines act as a momentum sink on the mean flow transferring a fraction of the kinetic energy into electricity and the rest into turbulent kinetic energy. The latter represents the mixing of the ambient flow by the turbines.

The following physics parameterizations are selected: Goddard (six-class) Cloud Microphysics Scheme (Tao et al., 1989); Rapid Radiative Transfer Model for Global Circulation Model Applications (Iacono et al., 2008) with climatological aerosol distribution (Tegen et al., 1997) for both short-wave and long-wave radiation; Monin-Obukhov surface layer scheme (Monin and Obukhov, 1954) with the Mellor-Yamada Nakanishi and Niino level 2.5 Planetary Boundary scheme (Nakanishi and Niino, 2004, 2006); Noah land surface model (Chen and Dudhia, 2001); and Betts-Miller-Janjić (Janjić, 1994) cumulus scheme with precipitating convective cloud scheme (Koh and Fonseca, 2016). The WRF model configuration used in this work is the one found to give the best agreement with observed data at the Honkajoki site out of the different configurations considered for the month of April 2016.

Three domains were used in the WRF model experiments (Fig. 4). The setup of domains 1 and 2 are identical to the ones used by Wang et al. (2019). Domain 1 has a spatial resolution of 15 km and comprises the entire Scandinavian Peninsula (144×160 grid nodes). Domain 2 uses a 3 km resolution and includes most of the Botnia-Atlantica region (301×381 grid nodes). Domain 3 uses a 600 m resolution, centered over the Honkajoki wind park (96×96 grid nodes). The model has 60 vertical levels, spanning up to 30 hPa (~25 km). A higher vertical resolution in the Planetary Boundary Layer is used, with about 20 levels in the lowest 200 m. In domain 2 and 3, the cumulus parametrization scheme is not used and instead convection is explicitly resolved

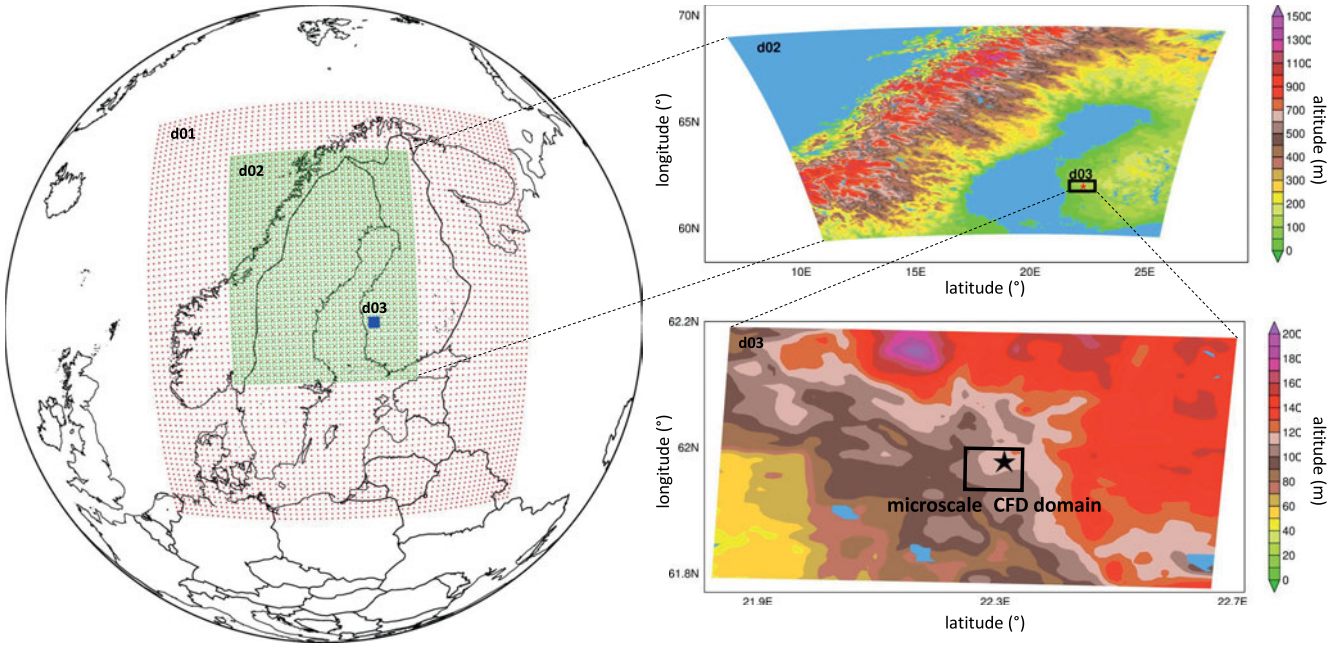

Figure 4: Spatial extent of domain 1 (d01), domain 2 (d02), domain 3 (d03) of the WRF model used in the simulations. The microscale CFD domain is indicated as a black rectangle in the lower-right panel. The sodar position is indicated with a star in the top- and bottom-right panels.

by the model. In domain 1, grid nudging towards CFSR is employed. The water vapor mixing ratio is nudged in the mid- and upper-troposphere while the horizontal wind components and potential temperature perturbations are nudged in the upper-troposphere and lower stratosphere. The nudging time-scale is set to 1 h for all variables.

In order to limit the accumulation of integration errors, following Lo et al. (2008), each month's run is broken into three overlapping 11/12-day periods with the first day regarded as model spin-up. For example, for March 2016 the model is run from 29th February to 11th March, 10th March to 21st March and 20th March to 1st April. The output is stored every 3 h, 1 h and 10 min for the domains 1, 2 and 3, respectively. For this work, the output of grids d02 and d03 are used.

The albedo, vegetation fraction and leaf area index used in the WRF simulations are derived from the National Oceanic and Atmospheric Administration Advanced Very High Resolution Radiometer (AVHRR) multi-year data (Csiszar and Gutman, 1999; Gutman and Ignatov, 1998). The other land surface parameters are assigned to each land category from a 1 km AVHRR data spanning April 1992 to March 1993 (Loveland et al., 2000). The terrain input used in the WRF runs is interpolated from a ~925 m spatial resolution dataset generated by the United States Geological Survey (USGS) that comes with the WRF pre-processor.

2.3 WindSim model

The CFD software WindSim is used to simulate the wind flow in the microscale model domain. The WindSim CFD model is based on RANS equations for momentum, turbulence and temperature, using the standard k-ε turbulence closure scheme. More information about the governing equations of the model are detailed in the works of Gravdahl (1998). To consider atmospheric stability effects in the atmosphere the potential temperature equation is solved explicitly. The change of the mean potential temperature is influenced by advection, thermal diffusion and turbulent heat transfer (Meissner et al., 2009). Forest is modelled in accordance to Busch (2017).The software solves the atmospheric steady-state flow for a given set of initial and boundary conditions through numerical methods. In this study, the Coriolis force is not included in the microscale modelling. Wind turbines are not explicitly represented in the microscale model. For energy calculations in Section 4.4, an analytical wake model is used to account for the impact of the wind turbines.

The digital terrain model has a horizontal spatial resolution of 20 m×20 m. In the vertical direction, the grid extends up to 450 m, with a finer vertical spatial resolution towards the ground, which has a grid size lower than 10 m for heights below 100 m a.g.l (Fig. 5). The modelled area is a rectangle of approximately 4.8 km×6.6 km, with the lower left corner at 565,498 m east 6,867,799 m north and the upper right at 570,318 m east 6,874,439 m north in the Universal Transverse Mercator coordinate system, Zone 34.

Data about the elevation and canopy of the site was retrieved from the National Land Survey of Finland (https://www.maanmittauslaitos.fi/en). This website provides laser altimetry data and various resolution altimetry models for most of Finland. The datasets retrieved from this website correspond to elevation model data with a horizontal resolution of 2 m and point-like laser scanning data depicting objects on the ground with

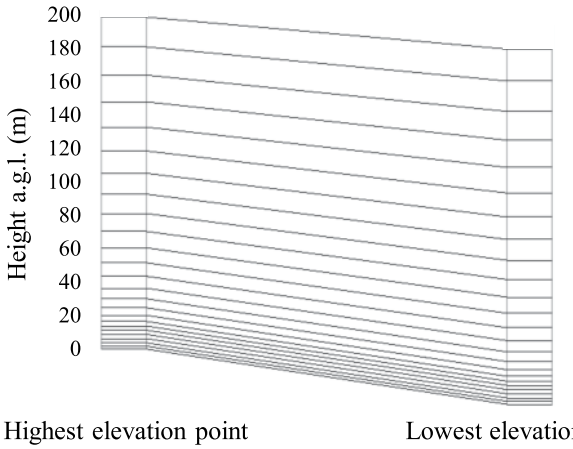

Figure 5: The left and right columns display a schematic view of the vertical grid distribution at the position with maximum and minimum elevation, respectively, in the CFD domain. For visualization purposes up to 200 m a.g.l. is displayed.

Table 3: Canopy height (h_c) ranges used to model the forest. For a given range, one canopy height and a number of cells are used to build the forest in the model.

Canopy height range (m)	Modeled Canopy height (m)	Number of grid cells used
$1 < h_c \leq 2.5$	1.75	1
$2.5 < h_c \leq 5$	3.75	2
$5 < h_c \leq 7.5$	6.25	3
$7.5 < h_c \leq 10$	8.75	4
$10 < h_c \leq 12.5$	11.25	5
$12.5 < h_c$	13.75	6

their respective horizontal and vertical coordinates. The data was retrieved in December 2018. Both datasets were aggregated into the 20 m resolution grid of the CFD model. The canopy height was obtained by subtracting the elevation from the laser altimetry data and then used to model 6 layers of forest (Table 3). For canopy heights lower than 1 m it was assumed that no forest was present and therefore they correspond to grassland. By visual inspection, for important areas of the site the aerodynamic roughness data was manually corrected, like farmlands, asphalt, residential areas and buildings (Fig. 6).

2.4 Validation methodology

In wind resource assessment studies, it is necessary to extrapolate measurements taken at one point, to the planned turbine positions in order to assess the wind energy potential. The horizontal and vertical transfer in space of those measurements need to be done either by analytical formulas or by 3-D models, like RANS CFD. For wind energy applications, RANS CFD model results are Reynolds number independent (Bachant and Wosnik, 2016; Berg et al., 2011). This means that wind flow relative perturbations caused by the orography are independent of the wind speed. In other words, the ratio between the wind speed values at two different locations of the simulated domain are independent of the wind speed. Such ratio is defined as the "speed-up ratio" and is the variable used to quantify the performance of the microscale model. Since the speed-up ratios depend only on the orography, they also depend only on the wind direction. In this study, 12 different wind directions are simulated, generating 12 sets of speed-up ratios.

The validation of the microscale model consists in first "transferring" the wind speeds from a reference measurement to the location of a target measurement (Fig. 7). The transferring is performed by multiplying the wind speeds at the reference, u_R, by the corresponding speed-up ratio, SU. For a given measured wind direction at the reference point α_R, the speed-up ratio is obtained by linearly interpolating the speed-ups of the two closest wind directions. For example, if the total number of simulated directional sectors, D, is 12 as in this study, and the measured direction is 15°, the SU is interpolated from the speed-ups modelled for wind directions 0° and 30°. The transferred values are compared to the measured wind speed at the target, u_T. The performance of the model is then quantified by the crosschecking prediction error, XPE, defined as:

$$XPE(R,T) = \frac{\sum_{t=1}^{N(R,T)} \frac{u_R(t)\cdot}{N(R,T)} \cdot \sum_{t=1}^{N(R,T)} \frac{SU(\alpha_R(t))}{N(R,T)} - \sum_{t=1}^{N(R,T)} \frac{u_T(t)}{N(R,T)}}{\sum_{t=1}^{N(R,T)} \frac{u_T(t)}{N(R,T)}} \quad (2.1)$$

$N(R,T)$ is the total number of concurrent measured timesteps t between the reference R and the target measurement T, and α_R is the measured wind direction at the reference point. In contrast to validation metrics used in WRF or Unsteady RANS models, where deterministic values are compared, the objective of the XPE is to validate the simulated speed-up ratios and not the simulated wind speed values.

Crosschecking prediction errors can also be obtained for a particular directional sector, in which case is denoted as $XPE_\Lambda(R,T)$, with $\Lambda = \{(i-1)\cdot 360°/D,\ i = 1,\ldots,D\}$. In this case, the same expression as in equation (2.1) is used, with the summation limited to α_R values within the range $[\Lambda - 360°/2D, \Lambda + 360°/2D]$, in which case the total number of concurrent timesteps is denoted as $N_\Lambda(R,T)$.

3 Meso-to-microscale coupling methodology

The WRF simulations results are used to drive the microscale wind flow model. Representative WRF fields are generated for different atmospheric stability conditions and wind directions by averaging the WRF data. These averaged fields are used to generate the initial and boundary conditions of the CFD model. The averaging and transferring methodologies are detailed in the following subsections.

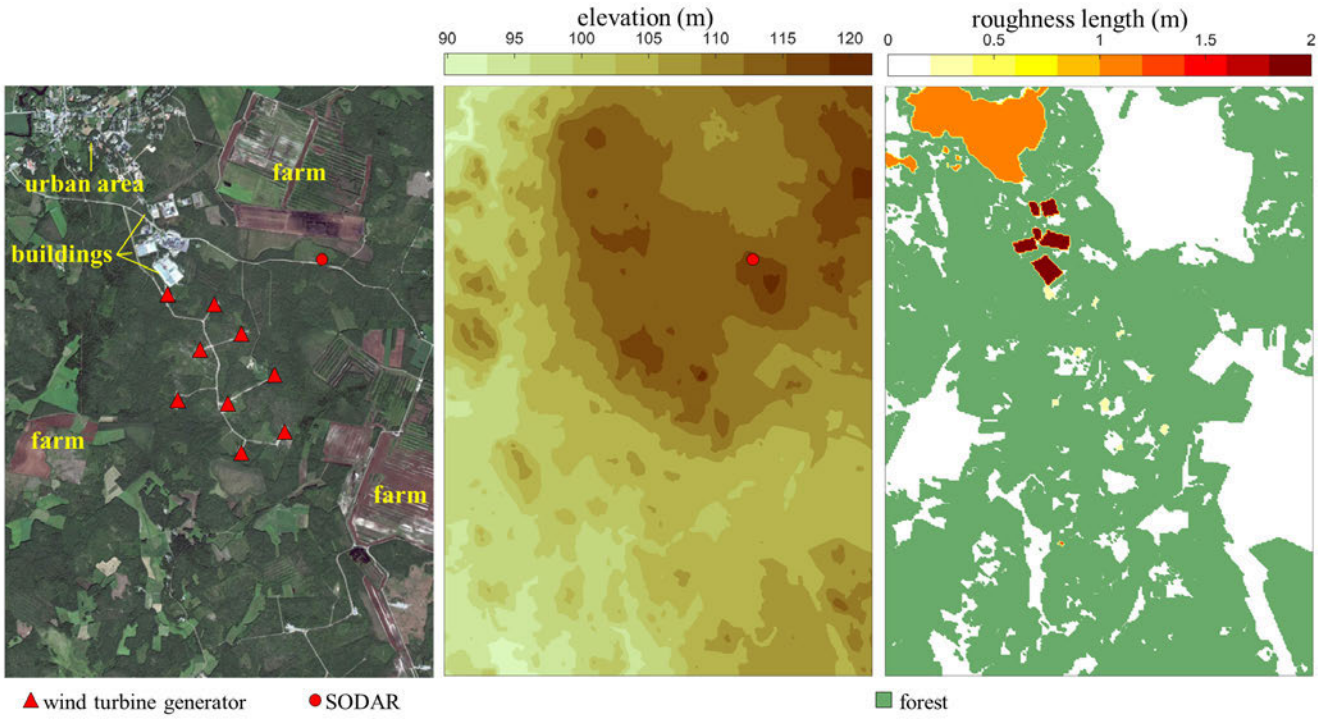

Figure 6: Satellite image (left), elevation (center) and aerodynamic roughness length (right) of the CFD digital model. In the satellite image the position of the wind turbines of the Honkajoki windfarm is shown as well as relevant areas in the domain.

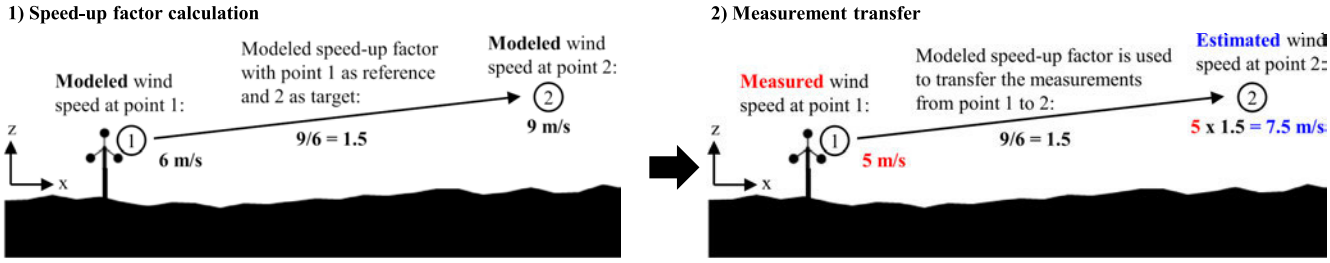

Figure 7: Example of measurement transfer using RANS CFD model results.

3.1 Calculation of representative atmospheric conditions

The meso-microscale coupling could be conducted by running one microscale simulation for each timestep of the WRF data. With this procedure, the estimation of the annual energy production of a wind energy project would require 8760 steady-state simulations for hourly WRF data. This high demand of computational resources is prohibitive in the industry, and therefore, a method to generate representative boundary conditions has been proposed.

The developed methodology consists in generating one representative mesoscale field per wind direction and/or per atmospheric stability condition, from the 1-year WRF simulation. These fields are computed by averaging all WRF data with the same representative main wind direction and atmospheric stability. The main wind direction is determined by averaging the wind directions of all WRF grid-points at the inlets of the microscale domain between 60 m and 160 m a.g.l. By using this procedure, it is expected that the main mesoscale conditions at the heights of interest for wind energy generation can be captured.

When atmospheric stability is considered, the representative atmospheric stability is estimated from the shear exponent of one vertical profile of horizontal wind speed (Sutton, 1949). This profile is obtained by averaging in the horizontal direction the wind speeds of all WRF grid-points inside the CFD domain. All vertical levels between 50 and 100 m are used to compute the shear exponent. The thresholds used to classify the atmospheric stability are based on the work of Wharton and Lundquist (2012) and the reference therein. Shear exponents <0.1 are considered unstable, >0.2 are considered stable and between those two thresholds it is considered neutral.

In this work, two versions of the proposed coupling methodology are used, one without considering atmospheric stability, here referred as to “all-stabilities”, and

the other considering three atmospheric stability classes: unstable, neutral and stable. All-stabilities simulations correspond to the average of all WRF timesteps throughout the year for a given wind direction, whereas the other simulations average the WRF timesteps throughout the year that belong to a particular stability class. The averaging procedure is conducted for each of the 12 directional sectors, yielding a total of 12 WRF fields for each of the four cases.

The averaging is conducted at each grid-point of the WRF domain. The following variables from the WRF model are considered in the coupling: (i) wind velocity vector, (ii) potential temperature, (iii) boundary layer height and (iv) friction velocity. These variables are directly averaged except for the horizontal components of wind speed and friction velocity. In the case of horizontal wind speed, magnitude and direction are averaged instead. Then the horizontal components of the wind are calculated by projecting the averaged horizontal wind speed according to their averaged direction. On the other hand, the averaged friction velocity is computed using the root mean square of the friction velocities.

3.2 Boundary conditions for CFD simulations

In RANS CFD simulations the values of all variables are iteratively re-calculated inside domain until they converge to a stable solution. This iterative procedure starts from a set of initial values which, in the case of steady-state CFD simulations, are fixed at the lateral and top boundaries during the whole simulation. The prescribed variables are the horizontal wind speed u, potential temperature θ, turbulent kinetic energy (TKE), k, and its energy dissipation rate (EDR), ε. In this study, two sets of initial and boundary conditions are used: 1) standalone and 2) coupled. For standalone simulations, the boundary conditions are computed from analytical profiles. For coupled simulations, wind speed and potential temperature are directly interpolated from the WRF model, while TKE and EDR are calculated using variables derived from the WRF model, in a similar fashion as Duraisamy (2014). One year of WRF output is used to generate the boundary conditions for the coupled simulations. Each of these simulations is compared with standalone simulations using similar wind direction and atmospheric stability.

3.2.1 Standalone CFD simulations

Analytical profiles are prescribed for every given wind direction. These profiles are derived from the Monin-Obukhov similarity theory in Han et al. (2000):

$$u(z) = \begin{cases} \frac{u_*}{\kappa}\left[\ln\left(\frac{z}{z_0}\right) - \psi_m\left(\frac{z}{L}\right) + \psi_m\left(\frac{z_0}{L}\right)\right] & , z \le h \\ u_G & , z > h \end{cases} \quad (3.1)$$

$$\theta(z) = \theta_0 + \frac{\theta_*}{\kappa}\left[\ln\left(\frac{z}{z_{h0}}\right) - \psi_h\left(\frac{z}{L}\right) + \psi_h\left(\frac{z_{h0}}{L}\right)\right] \quad (3.2)$$

$$k(z) = \begin{cases} \frac{u_*^2}{\sqrt{C_\mu}}\left(1 - \frac{z}{h}\right)^2 & \begin{matrix} z \le h; \\ , L < -200; \\ L > 0 \end{matrix} \\ \left(\begin{matrix} 0.36+ \\ 0.9\left(\frac{z}{h}\right)^{2/3}\left(1 - 0.8\frac{z}{h}\right)^2 \end{matrix}\right) w_* & \begin{matrix} z \le h; \\ , -200 < L < 0 \end{matrix} \\ 0 & , z > h \end{cases} \quad (3.3)$$

$$\varepsilon(z) = \begin{cases} \frac{u_*^3}{\kappa z}\left(1.24 + 4.3\frac{z}{L}\right)\left(1 - 0.85\frac{z}{L}\right)^{3/2} & , z \le h; L > 0 \\ \frac{w_*^3}{h}\left(0.8 - 0.3\frac{z}{L}\right) & , z \le h; L < 0 \\ 0 & , z > h \end{cases} \quad (3.4)$$

$$w_* = \left(\frac{g}{\theta_0}(\overline{w\theta})h\right)^{1/3} \quad (3.5)$$

$$\psi_m = \begin{cases} -5\frac{z}{L} & , \frac{z}{L} \ge 0 \\ 2\ln\left(\frac{1+x}{2}\right) + \ln\left(\frac{1+x^2}{2}\right) & , \frac{z}{L} \le 0 \\ -2\arctan(x) + \frac{\pi}{2} & \end{cases} \quad (3.6)$$

$$\psi_h = \begin{cases} -5\frac{z}{L} & , \frac{z}{L} \ge 0 \\ 2\ln\left(\frac{1+x^2}{2}\right) & , \frac{z}{L} \le 0 \end{cases} \quad (3.7)$$

$$x = \left(1 - 16\frac{z}{L}\right)^{1/4} \quad (3.8)$$

$$L = -\frac{\theta_0 u_*^3}{\kappa g(\overline{w\theta})} = \frac{\theta_0 u_*^2}{\kappa g \theta_*} \quad (3.9)$$

Here u_* is the friction velocity, u_G is the geostrophic wind, z_0 is the roughness length, h is the atmospheric boundary layer height, κ (= 0.4) is the Von Karman constant and L is the Monin-Obukhov length. The convective velocity scale, the gravitational acceleration, the reference temperature and the surface sensible heat flux are denoted as w_*, $g\theta_0$ and $(\overline{w\theta})$ respectively. ψ_m and ψ_h are the stability correction functions for wind speed and potential temperature, respectively (Businger et al., 1971; Dyer, 1974). It is assumed $z_{h0} = 0.1 z_0$ (Garratt, 1992). If neutral conditions are considered, the friction velocity is computed by enforcing $u(h) = u_G$ in equation (3.1). Otherwise, the friction velocity is obtained from a prescribed reference speed u_{ref} at a certain height z_{ref} by $u(z_{\mathrm{ref}}) = u_{\mathrm{ref}}$. The values of θ_* and $(\overline{w\theta})$ are computed from equation (3.9). At the top boundary of the CFD model, a no-friction wall is prescribed. Wind direction is assumed to be constant with height.

3.2.2 Coupled CFD simulations

For coupled CFD simulations, wind speed and potential temperature boundary conditions are computed by interpolating and extrapolating the WRF values onto the microscale grid. Vertical interpolation is conducted using cubic spline interpolation and horizontal interpolation by linear interpolation. In the case of the wind speed, the interpolation is conducted with respect to

the height above ground level, whereas for the potential temperature it is conducted with respect to the height above sea level. For the grid cells of the microscale domain below the lowest vertical level of the WRF model ($z_{\sqcup}$), extrapolation is conducted using equations (3.10) and (3.11), where $u_{\sqcup}$ and $\theta_{\sqcup}$ are the wind speed and potential temperature at the lowest vertical level of the WRF domain. u_* is retrieved from the WRF model, L is computed using the gradient method (Arya, 1998), θ_* is computed from equation (3.2) and $(\overline{w\theta})$ is computed from equation (3.9).

$$u(z) = u_{\sqcup} - \frac{u_*}{\kappa}\left[\ln\left(\frac{z_{\sqcup}}{z}\right) - \psi_m\left(\frac{z_{\sqcup}}{L}\right) + \psi_m\left(\frac{z}{L}\right)\right] \quad (3.10)$$

$$\theta(z) = \theta_{\sqcup} - \frac{\theta_*}{\kappa}\left[\ln\left(\frac{z_{\sqcup}}{z}\right) - \psi_h\left(\frac{z_{\sqcup}}{L}\right) + \psi_h\left(\frac{z}{L}\right)\right] \quad (3.11)$$

Because interpolated values might not conserve mass in the microscale domain, mass conservation is enforced at the top and lateral boundaries. As done in Veiga Rodrigues et al. (2016), the correction factor ϕ_b for the normal velocities at the boundary b is calculated from equations (3.12) and (3.13). Here A_i is the grid area and S_b is the set of points belonging to the boundary $b \in [1, 5]$ (four lateral boundaries plus top boundary). $\dot{m}_b$ corresponds to the mass flow, where positive sign indicates that mass is flowing into the domain.

$$\phi_b = 1 - \mathrm{sgn}(\dot{m}_b)\frac{\sum_{k=1}^{5}\dot{m}_k}{\sum_{k=1}^{5}|\dot{m}_k|} \quad (3.12)$$

$$\dot{m}_b = \sum_{i\in S_b}\rho A_i u_{\perp,i} \quad (3.13)$$

TKE and EDR cannot be directly transferred from the mesoscale model to the microscale model. Coarser grids cannot describe smaller fluctuations of the wind flow, and therefore, the amount of TKE in a grid-box would be higher compared to a finer grid (Moeng et al., 2007). Therefore, TKE and EDR are computed using equations (3.3), (3.4) and (3.5) in a similar fashion as Duraisamy (2014). Here u_* and h are horizontally interpolated from the WRF domain.

4 Comparison of the coupled and standalone simulations

The methodology presented in Section 3 is used to produce representative WRF data for the previously defined atmospheric stability conditions: (i) all-stabilities, (ii) unstable, (iii) neutral and (iv) stable. The representative WRF fields of each of the 12 directional sectors are used to force the coupled microscale CFD models. In order to assess the improvement of the coupled methodology, the results are compared for each stability case with their corresponding standalone microscale simulations and the averaged WRF field.

Standalone simulations correspond to the standard application of CFD models in the wind industry for wind resource assessment. The values used to compute the boundary conditions of the standalone microscale simulations are presented in Table 4. These values were selected in order to have a good fit with the observed SODAR profile for each respective atmospheric stability case.

To calculate the simulation error of each atmospheric stability case, the measurements are also filtered according to the measured shear exponent between 50 and 100 m. The classification of measurements is performed over 30-min averages in order to reduce the noise. The same thresholds used in the classification of the WRF fields are used for the measurements. The frequency distribution of the atmospheric stability in the WRF simulations and measurements is presented in Fig. 8. Domain 2 and 3 of the WRF model have identical wind roses and therefore only the last is presented. The wind rose of the WRF simulations is quite similar to the measured one when all data is compared. This is also true for the stable case but not for the unstable and neutral case. Nevertheless, over the full year, the proportion of stability classes in the WRF simulations and SODAR is similar, with a slight over representation of neutral cases in the WRF model.

The main purpose of wind flow models is to extrapolate measured wind horizontally and vertically. Typically, measurements are conducted at about 60 to 120 m and vertically extrapolated to higher heights and/or horizontally extrapolated at places where wind turbines would like to be placed. For this reason, all comparisons in this section were conducted using the measured wind speed at 80 or 120 m as a reference. Only wind speeds above 3 m/s were considered for the calculation of the wind profiles and errors, since they are of interest for wind energy calculations. Only directional sectors with a frequency higher than 5.5 % (~15 days) are discussed in the following section. This assures that the discussion is based on observation with statistical significance.

4.1 Vertical profiles of horizontal wind speed

For each atmospheric stability case, the profiles of horizontal wind speed simulated at the SODAR position by the different approaches are compared. The approaches correspond to one set standalone simulations and two sets of coupled simulations. Each of these sets correspond to one simulation per directional sector. In addition, the averaged profile of the WRF d02 and d03 at the SODAR position are shown for each case. The profiles were scaled to match the SODAR wind speed at 80 m in order to validate the speed-up ratios, as discussed in the previous paragraph. This qualitative comparison is presented for the most frequent wind directions at 80 m for all-stabilities and stable cases (Fig. 9 and Fig. 10). The number of occurrences for the neutral and unstable case are very low, therefore only the sector with the highest frequency will be shown (Fig. 11).

When all stabilities are considered (Fig. 9) there are not important differences between the coupled and stan-

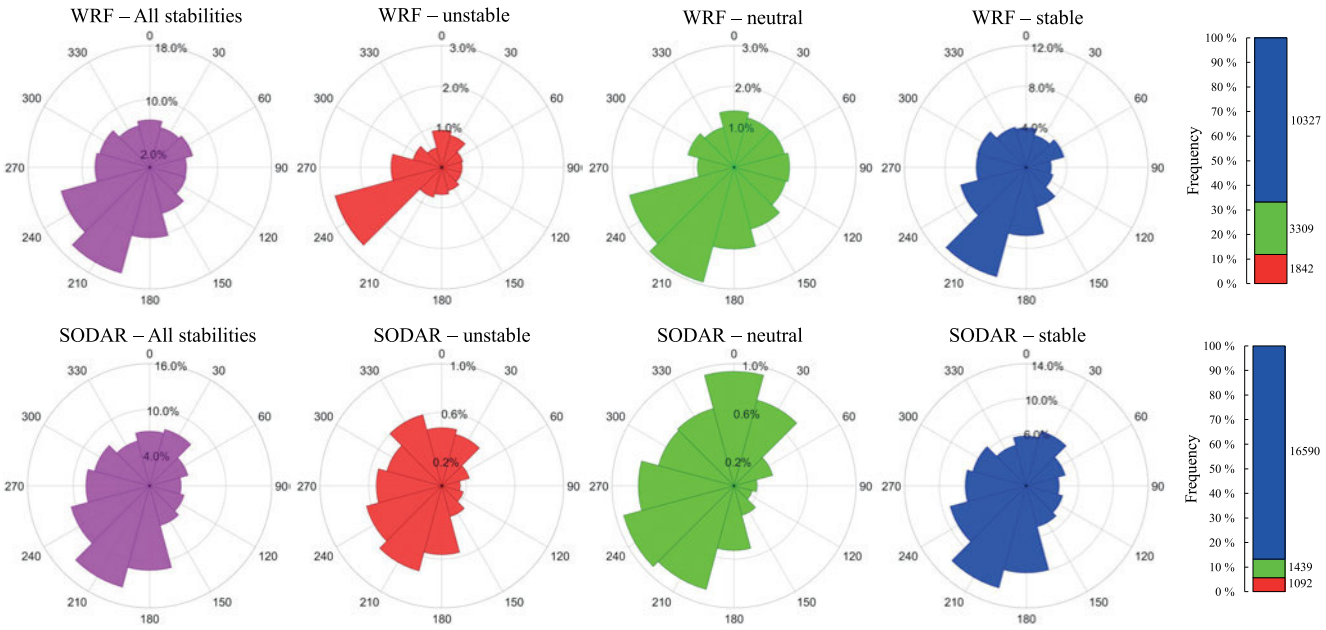

Figure 8: Wind roses of the representative direction of the WRF d03 timesteps (top) and of the measured wind at 100 m by the SODAR (bottom) for the different stability classes: all stabilities (magenta), unstable (red), neutral (green) and stable (blue). In the right panels the frequencies of the stability classes within the simulated and measured period, respectively, are displayed. Next to the bars, the number of 30-min timesteps per stability is shown.

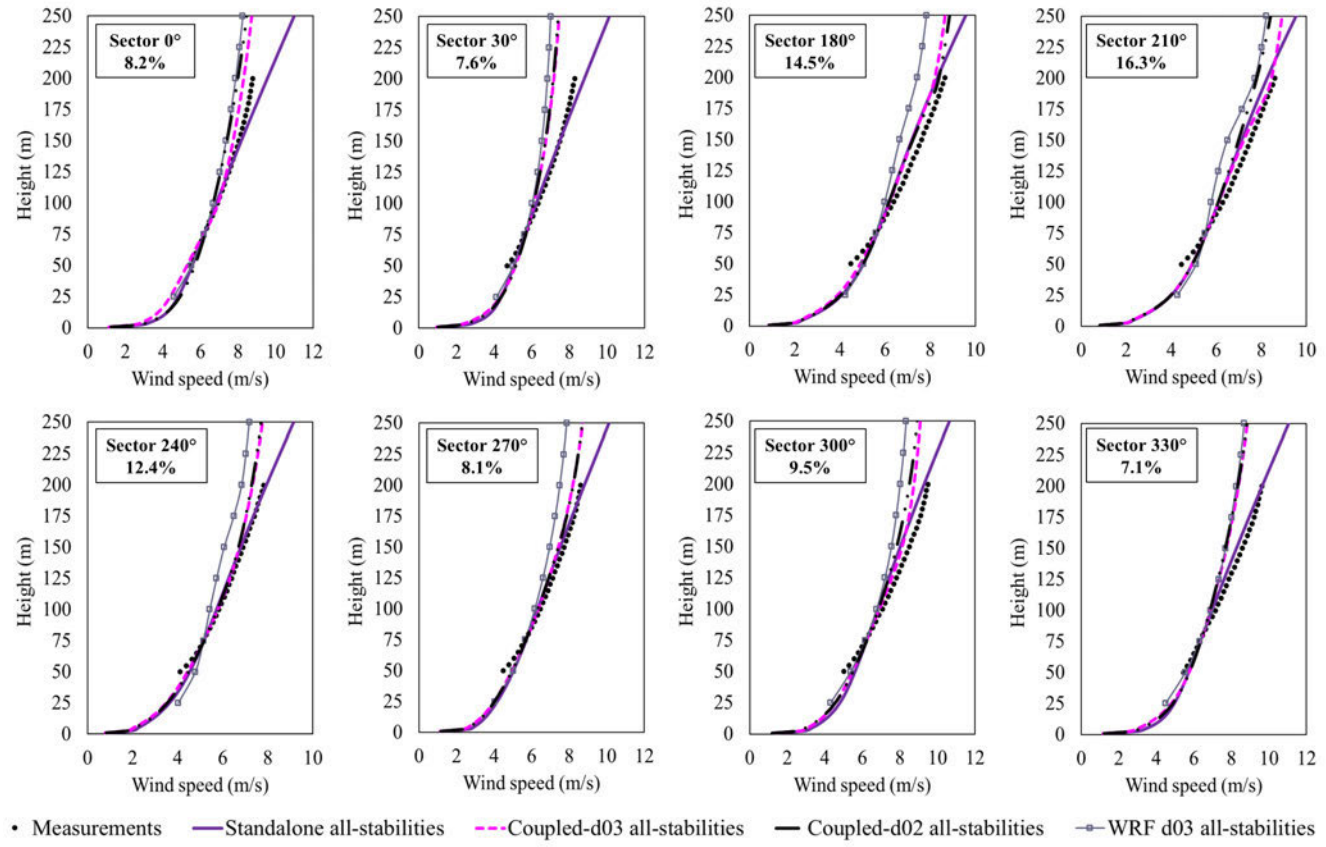

Figure 9: Simulated horizontal wind speed vertical profiles for the main wind directions for all stabilities. Standalone, coupled and WRF simulated profiles are shown. At the top-left corner of each panel, the directional sector and its frequency is displayed. Coupled-d02 and Coupled-d03 are forced using WRF output from grids d02 and d03, respectively.

Table 4: Prescribed physical parameters used to compute the boundary conditions of each standalone microscale simulation.

Atmospheric stability condition	Input variables				
All stabilities	$u_{ref} = 6.13$ m/s	$z_{ref} = 100$ m	$h = 400$ m	$\theta_0 = 280$ K	$L = 150$ m
Unstable	$u_{ref} = 4.39$ m/s	$z_{ref} = 100$ m	$h = 1000$ m	$\theta_0 = 280$ K	$L = -200$ m
Neutral	$u_G = 6.30$ m/s		$h = 500$ m		
Stable	$u_{ref} = 6.26$ m/s	$z_{ref} = 100$ m	$h = 400$ m	$\theta_0 = 280$ K	$L = 100$ m

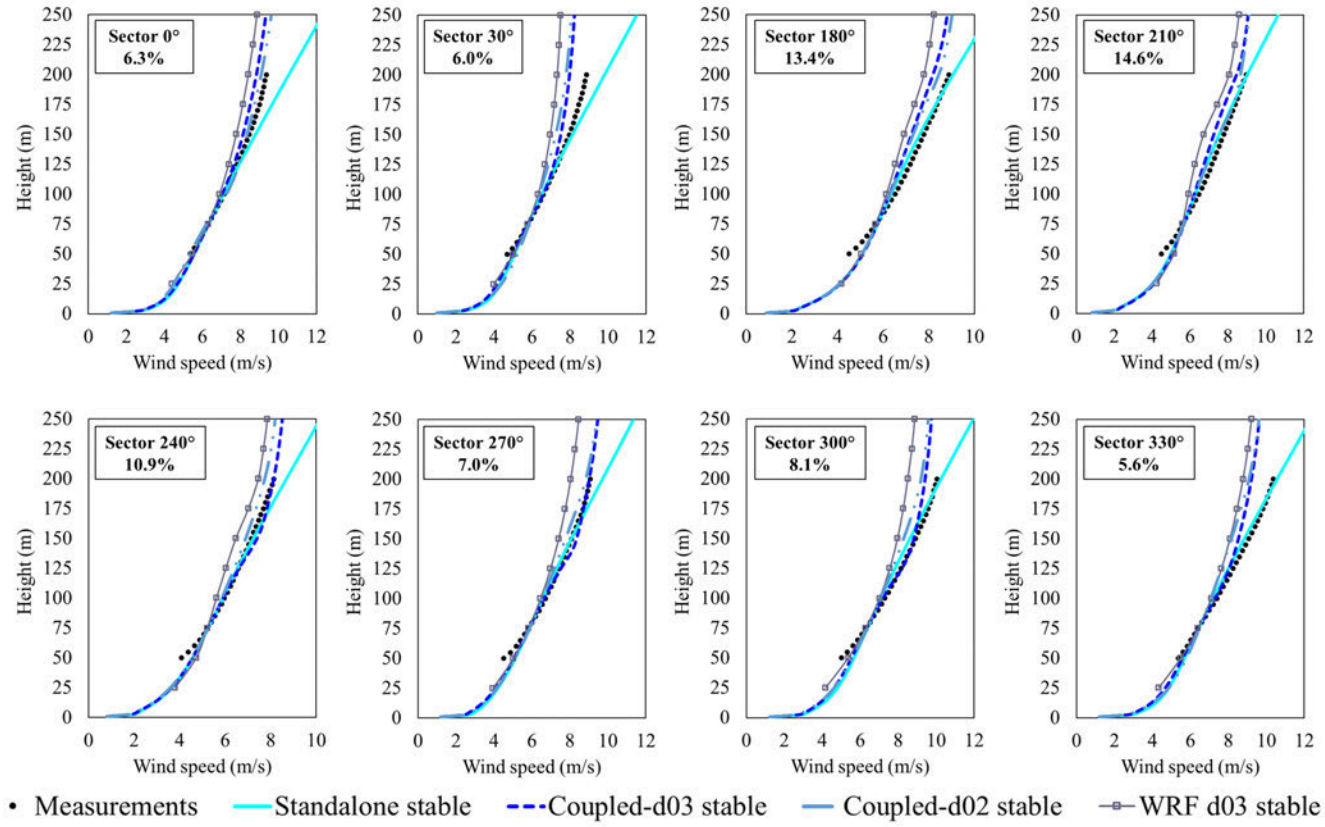

Figure 10: Same as Fig. 9 but for stable atmospheric conditions.

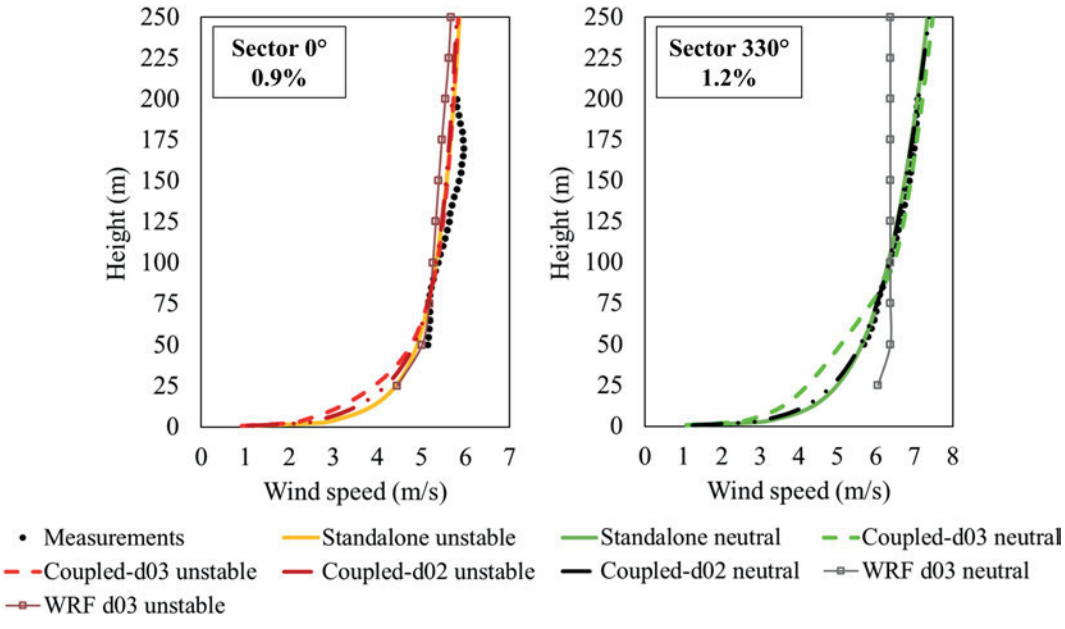

Figure 11: Same as Fig. 9 but for unstable (left) and neutral (right) atmospheric conditions.

dalone approaches. In some sectors, the coupled simulations present a better performance (sectors 0° and 210°), in some sectors the standalone profiles fit better (sectors 30°, 240°, 330°) and for some sectors, they can be quite similar (sectors 180°, 270°, 300°). In most of the presented sectors, differences are rather small. In addition, for most sectors the microscale simulations present a better performance compared with the profile obtained from the WRF model. It is interesting to note that there is not a big difference between the coupled simulations forced by the WRF outputs from d02 and d03.

Despite these inconclusive results, it is important to highlight that coupled simulations tend to present a more realistic shear for heights above 150 m. Standalone simulations presents a rather high and constant shear above 80 m. In the coupled simulations, the shear decreases towards higher heights, which is also seen in the measurements. It is then expected that coupled simulations have a better performance when extrapolating measurements to higher heights. Standalone simulations cannot reproduce this since their boundary conditions use wind speed profiles assuming that Monin-Obukhov similarity theory is valid up to the boundary layer height.

For stable simulations (Fig. 10), the coupled simulations are as good or better than the standalone approach for sectors 0°, 30°,180°, 210°, 240° and 270°. In sectors 0°, 240° and 270° the improvements are important. In most sectors, both coupled sets of simulations behave similarly. Nevertheless, the one forced by the highest resolution WRF output (d03) presents a lower performance for sectors 240° and 270°. For all sectors, the direct use of the WRF output gives worse results, as the shear is lower than the measured one. The most probable reason for the lower shear is that in stable cases the wake from the wind farm is sustained longer and therefore underestimating the wind speed.

In the same way as when all stabilities were considered, standalone simulations present a high and constant shear above 80 m. This is not the case for the coupled simulations, which present a more realistic shear at higher heights. In addition, the coupled simulations using the WRF d03 output shows a change in the shear at 150 m in sectors 240°, 270° and 300°. Nevertheless, this cannot be seen in the measurements.

The number of occurrences for unstable and neutral cases is too low in order to draw conclusions (Fig. 11). Especially for the unstable case, where the averaged profile of wind speed does not follow a power law behavior. In the neutral case, the microscale models can reproduce a neutral profile, with the exception of the coupled simulations using the d03 domain. This indicate that the profile obtained from the WRF d03 is not proper, whereas the one from d02 is. This suggest that going from a 3 km resolution to 600 m might not necessarily improve WRF simulation results in a flat area.

In overall, there are differences between the profiles simulated by the coupled and standalone approaches when they are compared to the measurements, depending on the analyzed directional sector. Considerable improvements from the coupled approach was obtained in some cases, especially for stable conditions. Nevertheless, the limited improvement is in part expected given the simplicity of the terrain. Flat sites can be easily be modelled different atmospheric stabilities by just adjusting the shear at the inlet (as done in the standalone simulations), as long as there are no complex weather patterns in the site. In addition, as seen in Fig. 9 and Fig. 10, the wind speed profile of some sectors are not properly captured by the WRF simulations.

Coupled simulated profiles show a more realistic shear at higher heights. In the case of the stand-alone simulations, the profiles tend to have a constant shear above 80 meters, whereas in the coupled simulations the shear changes above 150 m. In particular for the stable case, there is a notable increase in the wind shear above 50 meters and a decrease above 150 meters. This is an expected shape for a stable atmosphere. The WRF model reproduces this profile and it is transferred to the microscale simulation through the proposed methodology.

For the directional sectors 0°, 30°, 300° and 330°, the simulated shear presented in Fig. 9 and Fig. 10 is considerably lower than the measured one. This reduced shear is not caused by the wake simulated by the WRF model since the wind farm is situated southwest of the SODAR position. Therefore, measurements could only be affected by the wake when the wind is coming from the directional sectors 180° to 270° (see Fig. 6). A possible explanation is that the WRF simulations do not properly reproduce the average shear of these sectors given their low frequency. In fact, all of these directional sectors have a frequency lower than 8 % (Fig. 8).

4.2 Cross-check prediction errors

In order to quantitatively assess the simulated vertical profiles with respect to the observed data, the sector-wise crosschecking prediction errors (XPE_Λ) are used. In order to study the performance of the models in the typical context of wind resource assessment, errors are calculated using the measured wind speed by the SODAR at 80 m as a reference and measurements at 120 m which equals the hub height of the turbines (Table 5). It is also of interest to compare the performance of the models at higher heights close to the tip of the turbines. For this reason, errors are also calculated using 120 m as a reference and 200 m as a target (Table 6). As previously discussed, unstable and neutral cases will not be discussed given their low occurrence.

When using 120 m as a target and all stabilities are considered, the coupled simulations forced with the WRF d03 presents slight improvements compared with the standalone approach for sectors 180° to 300°. This improvement has an average of 0.78 % and a maximum for 300° of 1.52 %. Standalone simulations perform significantly better for sectors 30° to 120°. Nevertheless, these sectors correspond to some of the least frequent

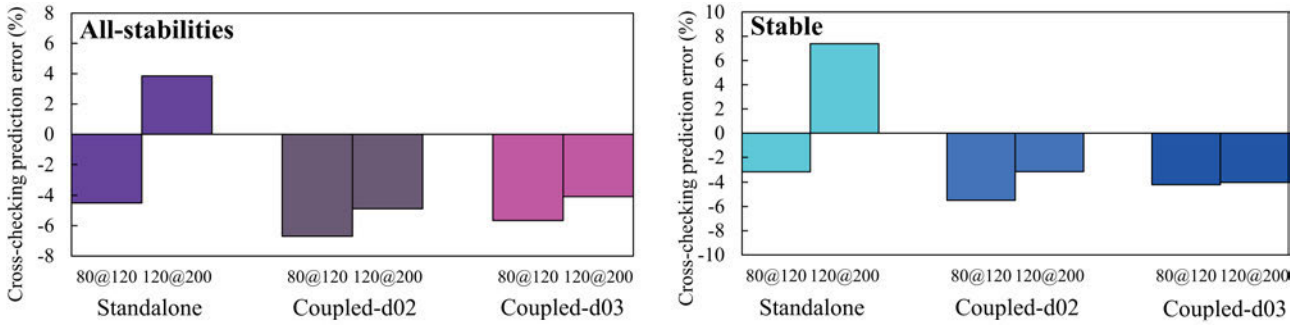

Figure 12: Total crosscheck prediction error. In each panel, the atmospheric stability condition is shown in the top-left corner. X@Y corresponds to the error using X m as reference and Y m as a target measurement.

Table 5: Sectorwise crosschecking prediction error using the wind speed measured by the SODAR at 80 m as a reference and 120 m as a target, for all microscale simulations. Darker colors represent higher frequencies and errors. Model errors are colored in red for overprediction and in blue for underprediction. SA: standalone, CPd02: coupled with WRF d02 and CPd03: coupled with WRF d03.

Directional	Error (%) – all stabilities				Error (%) – stable			
sector	Freq.	SA	CPd02	CPd03	Freq.	SA	CPd02	CPd03
0	3445	-2.06	-7.02	-2.92	2839	-0.89	-0.14	-3.61
30	3686	-3.97	-9.07	-9.01	3213	-2.34	-8.17	-4.09
180	5778	-5.14	-4.41	-4.48	5432	-3.77	-5.58	-5.92
210	6777	-5.18	-5.75	-4.46	6179	-4.44	-4.26	-5.68
240	5356	-3.08	-2.73	-2.19	4803	-1.89	-3.54	-0.21
270	3853	-2.75	-2.93	-2.63	3443	-1.74	-3.47	1.23
300	4070	-5.72	-6.38	-4.20	3590	-4.42	-6.01	-0.81
330	3093	-4.60	-8.27	-8.07	2521	-3.99	-7.07	-4.05

Table 6: Same as Table 5 but using SODAR measurements at 120 m as reference and 200 m as target.

Directional	Error (%) – all stabilities				Error (%) – stable			
sector	Freq.	SA	CPd02	CPd03	Freq.	SA	CPd02	CPd03
0	2623	9.03	-4.11	-4.71	2063	11.60	-4.46	-3.83
30	2909	6.85	-8.45	-8.22	2399	10.02	-7.56	-9.47
180	4385	2.31	4.72	2.13	4056	6.82	2.45	-0.81
210	6433	0.48	-5.06	1.73	5857	4.49	0.03	0.07
240	5428	2.91	-5.80	-6.16	4783	6.78	-3.01	-1.49
270	3130	5.78	-1.64	-1.66	2753	9.40	0.74	-1.61
300	3091	3.60	-5.33	-4.70	2618	6.59	-3.49	-6.47
330	2468	4.15	-6.64	-6.75	1953	5.55	-5.83	-8.80

ones. Except for sectors 0° and 300°, the coupled simulations do not present important differences when forced by the d02 or the d03 of the WRF. This is consistent with the results presented in the previous subsection.

In the case of stable simulation results, significant differences among models are found for sectors 240°, 270° and 300°. For these sectors, error reductions of 1,7 %, 3 % and 3,6 % were obtained by using coupled simulations forced with the WRF d03 compared with the standalone results. This improvement is also seen when comparing between coupled simulations but with a lower magnitude. In these sectors, the high resolution WRF simulation seems to provide improvements for the coupled approach compared to the low resolution WRF simulation. The opposite happens for sector 30° and 180°, where the standalone simulations show a better fit to the measurements. The high variability in the performance of the coupled simulations indicates that the simulated shear by the WRF model between 80 and 120 m is very well reproduced in some sectors and very off for some others.

When using 200 m as a target and 120 m as reference, the performance of the models depends on the atmospheric stability. When all stabilities are considered, the overall performance of the models is similar. Nevertheless, for some individual sectors these differences can be significant. For example, in sectors 0° and 270° the both coupled models have an error reduction of about 4 %. The opposite happens in sectors 240° and 330° where the standalone model performs about 3 % better than the coupled one. The dependence of the model performances with the sectors indicates that the average shear might be modeled wrong for few sectors in the WRF simulations.

For stable simulations, the coupled models have the best overall performance. When the CFD is forced by the d02 of the WRF model, the error is on average reduced by 4.3 %, with a maximum reduction of 8.7 % in sector 270°. When forced with d03, the average error reduction is 4,1 % with a maximum reduction of 7.8 %, also in sector 270°. Despite the coupled models perform similarly, the sector in which they perform better are different. It is interesting to note that standalone simulations overpredict the wind for all directional sectors while the opposite happens for the coupled approaches. This reflects the limitation of the near-to-constant shear simulated by the standalone model. Since the shear is not reduced at higher heights (as in the coupled model) the wind is overpredicted.

In order to compare the overall performance of the models, the $XPE(R,T)$ are presented in Fig. 12. Overall, the standalone model performs about 2 % better than the coupled model at heights below 120 m. For heights above 120 m, both approaches perform similar when all stabilities are considered. If only stable cases are taken into account, then the coupled models perform about 4 % better. Given the shape of the profiles shown in Section 4.1, it is expected that the use of higher heights as reference give a better result for the coupled models. The reason is that in the coupled models the

shear is better represented at higher heights, while in the lower heights the opposite occurs.

The improvement of using d03 instead of d02 is rather small. Therefore, there is no need to increase the resolution of the WRF model, if the objective is to obtain averaged profiles in a flat site. It is important to note that these metrics serve to evaluate the simulated vertical profiles only for the heights for which measurements are available. It does not take into account the wind flow at higher heights, nor the validity of horizontal flow patterns what will be discussed in Section 4.3.

4.3 Horizontal wind speed patterns

In addition to different simulated vertical profiles of horizontal wind speed, it is expected that different boundary conditions produce different horizontal wind speed patterns. In order to compare such patterns, the 120 m horizontal wind speed of sector 210° is presented for the whole domain for the standalone, coupled and WRF models (Fig. 13). In order to facilitate the comparison of the speed up factors, the wind speeds are normalized by the wind speed at the lower left corner of the domain. For the microscale simulations, no wake is visible as it is not explicitly resolved in the CFD model. Only in the domain d03 of the WRF model it is visible. Nevertheless, it has no effect in the coupled CFD results. When wake calculations are needed in the microscale (as in Section 4.4) analytical formulas were used.

The patterns are quite different between the coupled and standalone simulations. In both approaches, for all stabilities, neutral and stable cases, there is a decrease of the wind speed in the downstream side of the domain. In the coupled simulations, the decrease is much stronger than in the standalone model. This higher decrease in the coupled simulations is due to increased turbulence around 120 m in that area caused by the forest. Differences in simulated turbulence is affected from a series of factors like friction velocity, boundary layer height and atmospheric stability.

It is expected that different stability conditions will generate different wind patterns. The coupled simulation presents such dependency, when comparing the unstable case with the stable or neutral ones. Such dependency is not seen in the standalone case, whose patterns have similar shape, despite the values of the increase and decrease of the wind speed varies.

Given the low resolution of the WRF model, their simulations do not present the microscale flow features seen in the CFD models. In the later, small speed up areas matching the elevation of the terrain can be seen scattered in the domain. Nevertheless, given the lack of measurements located at different positions inside the CFD simulation domain, it is not possible to validate such features. Also, it is not possible to evaluate which of the microscale models have a better representation of them. Finally, there are no major differences in the patterns generated by the coupled simulations forced by the domains d02 or d03 of the WRF model. As discussed in Sections 4.1 and 4.2, this indicates that there is no need to use resolutions higher than 3 km in non-complex areas.

4.4 Energy production

The CFD results are used to estimated energy production of the Honkajoki wind farm. The production is estimated by transferring a reference measurement to the positions of the wind turbines (see Figure 7). The frequency distribution of the transferred wind speeds is translated into energy output through the power curve presented in Fig. 14. The power curve is based on the turbine model Nordex N117/2400 with a hub height of 120 m. Wake losses are estimated using Jensen's analytical wake model (Katic et al., 1987) which uses as input the drag coefficient presented in Fig. 14.

The transferred wind speeds are calculated by using the speed-up ratios obtained from the standalone and coupled results. The models that considers only one atmospheric stability are only valid for measurements with that stability. Therefore, to compare them with the all-stabilities cases, their estimated energy production is weighted averaged by their frequency. As before, the SODAR at 80 m was used as a reference measurement to compute the speed-up ratios. The capacity factor estimated for each model is presented in Fig. 15.

The estimated production, as well as the wake losses, are very similar among the standalone and coupled simulations. The main reason is that the energy production calculation is based on the SODAR at 80 m. This measurement is first vertically extrapolated to 120 m and then horizontally extrapolated to the turbine positions. As seen is Section 4.2, the speed-up ratio from 80 m to 120 m at the SODAR position is not that different among models. The same is expected for the horizontal speed-ups since the terrain is flat. Given these conditions, it is also expected that the estimated energy production is relatively similar.

5 Conclusions

The performance of coupled simulations depends on the studied atmospheric stability and directional sector. When all stabilities are considered, the coupled model forced by the d03 of the WRF model perform similarly to the standalone simulations. In the case of stable conditions, the coupled simulation have an error reduction of 4 % for heights above 120 m. When the coupled model was forced with the d02 of the WRF model instead, the improvement in the stable case was similar for these heights. Nevertheless, the standalone performed 1.5 % better when all stabilities taken into account. These differences did not have a big effect in the estimated energy production.

The shear obtained from the coupled models at higher heights tends to be more realistic. The reason is

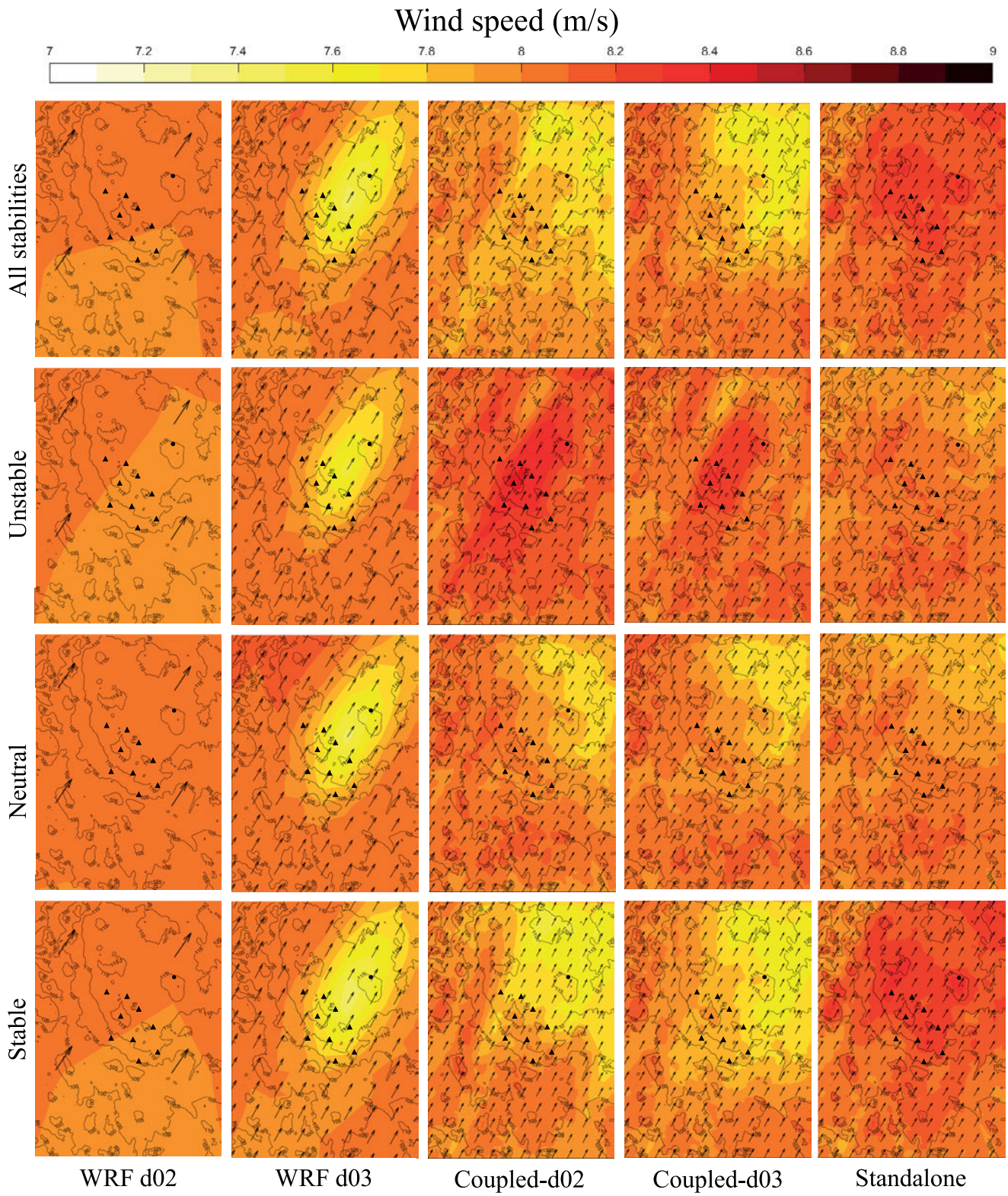

Figure 13: Simulated wind speed patterns for directional sector 210° at 120 m above ground. The corresponding atmospheric stability and type of simulation is indicated at the left and bottom side of the figure, respectively. Values are normalized by the simulated wind speed at the lower left corner and multiplied by 8 m/s. In all panels, the contours of the CFD elevation is displayed as black lines with a number indicating their elevation in meters. The black arrows indicate the direction of the wind for that node in the simulation. For CFD simulations, some arrows were skipped for visualization purposes. The position of the wind turbines are indicated with black triangles and the position of the SODAR with a black dot.

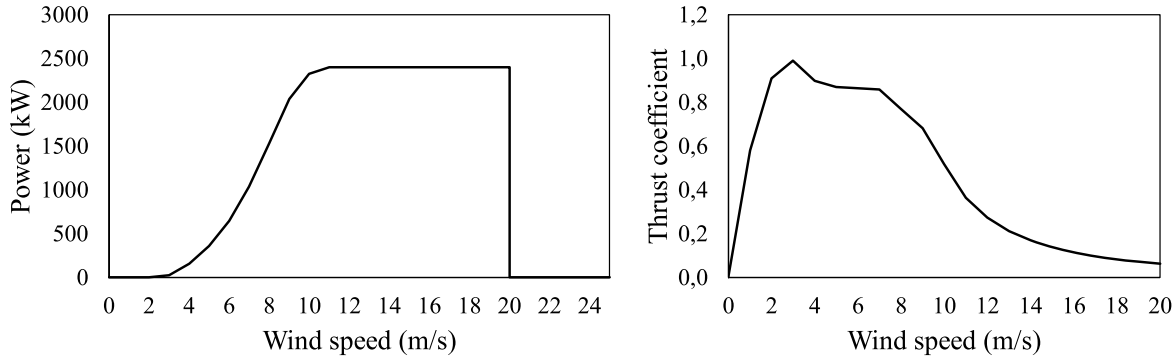

Figure 14: Power curve (left) and thrust coefficient (right) for the Nordex N117/2400 turbine with an air density of 1.225 kg/m^3.

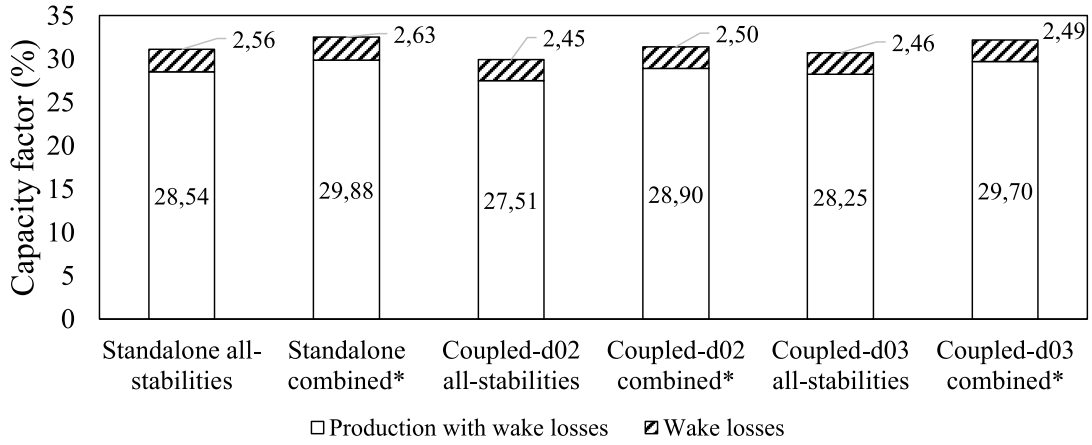

*weighted average of unstable, neutral and stable simulations

Figure 15: Estimated production of the Honkajoki wind farm by the standalone and coupled models, using the SODAR at 80 m as a reference measurement.

that WRF simulations provide information about the local atmospheric conditions in the area. This is more advantageous than the standalone approach that assumes Monin-Obukhov similarity theory all the way up in the boundary layer and constant wind speed above. This characteristic of the coupled profiles is very important as the trend is that wind turbine hub heights get higher for wind project development.

It is possible to further improve standalone simulations by tuning the parameters which are used to prescribe the boundary condition. For example, to get higher shear, the Monin-Obukhov length could be reduced, the boundary layer height could be lowered, the geostrophic wind could be increased, or a combination of these. The proposed methodology skips this tuning, preventing a subjective choice of such variables by indirectly including them in the shapes of the wind speed and temperature profiles interpolated from the WRF domain. Furthermore, such tweaking could only be conducted to match just one measurement position at the time, which does not guaranty a match for other positions.

Since the terrain of the modelled site is flat, it is expected that the CFD results depend mostly on the boundary conditions. This implies that any deviation in the WRF model results will have a big influence in the microscale results. The reason is that the corrections done by the microscale model are limited given that the orography does not play an important role, and only forest and roughness length changes influence the wind. For some directional sectors the averaged WRF simulated profile is not able to reproduce the shear seen in the measurements. These are the same sectors in which the coupled simulations have a lower performance. It is noted that this mainly happens in the least frequent directional sectors. This might indicate that in order to have on average a good reproduction of the shear in the WRF simulations, a relatively high frequency of occurrence is needed.

Independent of the results in terms of the vertical profiles, one of the expected gains from coupling with mesoscale models is to obtain more realistic horizontal wind patterns. In fact, in Section 4.3 was shown that the horizontal wind patterns are different between coupled and standalone models. Unfortunately, only the vertical profiles of horizontal wind speed of the CFD models could be validated due to the lack of observational data at different position than the SODAR. Even hav-

ing a good modelling of the vertical profiles, it is still possible to have poor horizontal modelling of the wind. Therefore, the methodology will now be applied to sites which have several measurement masts to understand the added value of the coupled simulations for simulating the horizontal wind speed patterns.

The results between the coupled models using the results from the WRF domains d02 and d03 are not significantly different. In the case of the vertical profiles, the results are similar for most sectors. Small differences can be found in few sectors, but any of the models performs consistently better. In the case of the horizontal patterns, the similarities are also high. Few differences can be found in some small pockets of the domain, but the overall pattern is the same. This result suggests that there is not an important gain in using higher resolutions in the WRF model when the terrain is flat. Nevertheless, in the case of complex sites, it is expected that such high resolutions are required to properly represent the topography, land use and small-scale flow features in the boundary layer.

Acknowledgments

This research was supported by a grant from The Norwegian Research Council, project number 271080. We acknowledge Botnia-Atlantica, an EU-programme financing cross border cooperation projects in Sweden, Finland and Norway, for their support of this work through the WindCoE project. We would like to thank the High Performance Computing Center North (HPC2N) for providing the computer resources needed to perform the numerical experiments presented in this paper. We would also like to thank the two anonymous reviewers for their useful comments.

References

Al-Yahyai, S., Y. Charabi, A. Gastli, 2010: Review of the use of numerical weather prediction (NWP) models for wind energy assessment. – Ren. Sustain. Energy Rev. **14**, 3192–3198, DOI: 10.1016/j.rser.2010.07.001.

Al-Yahyai, S., Y. Charabi, A. Al-Badi, A. Gastli, 2012: Nested ensemble NWP approach for wind energy assessment. – Ren. Energy **37**, 150–160, DOI: 10.1016/j.renene.2011.06.014.

Arya, S.P., 1998: Introduction to Micrometeorology, 2nd ed. – San Diego: Academic Press.

Bachant, P., M. Wosnik, 2016: Effects of Reynolds Number on the Energy Conversion and Near-Wake Dynamics of a High Solidity Vertical-Axis Cross-Flow Turbine. – Energies **9**, 73, DOI: 10.3390/en9020073.

Badger, J., H. Frank, A.N. Hahmann, G. Giebel, 2014: Wind-climate estimation based on mesoscale and microscale modeling: Statistical-dynamical downscaling for wind energy applications. – J. Appl. Meteor. Climatol. **53**, 1901–1919, DOI: 10.1175/JAMC-D-13-0147.1.

Baik, J., S. Park, J. Kim, 2009: Urban Flow and Dispersion Simulation Using a CFD Model Coupled to a Mesoscale Model. – J. Appl. Meteor. Climatol. **48**, 1667–1681, DOI: 10.1175/2009JAMC2066.1.

Berg, J., J. Mann, A. Bechmann, M.S. Courtney, H.E. Jørgensen, 2011: The Bolund Experiment, Part I: Flow Over a Steep, Three-Dimensional Hill. – Bound.-Layer Meteor. **141**, 219–243, DOI: 10.1007/s10546-011-9636-y.

Bilal, M., Y. Birkelund, M. Homola, M. Virk, 2016a: Wind over complex terrain – Microscale modelling with two types of mesoscale winds at Nygårdsfjell. – Ren. Energy **99**, 647–653, DOI: 10.1016/j.renene.2016.07.042.

Bilal, M., K. Solbakken, Y. Birkelund, 2016b: Wind speed and direction predictions by WRF and WindSim coupling over Nygårdsfjell. – J. Physics: Conference Series **753**, 082018, DOI: 10.1088/1742-6596/753/8/082018.

Boutanios, Z., C. Miller, H. Hangan, 2010: Computational analysis of the Manitoba September 5 1996 Storm: mesoscale WRF-ARW simulations coupled with microscale OpenFOAM CFD simulations. – In: The Fifth International Symposium on Computational Wind Engineering.

Busch, K., 2017: Application and Validation of the Forest Model inside WindSim CFD Software resp. Phoenics with the new GCV solver. – Master Thesis. Carl von Ossietzky Universität Oldenburg.

Businger, J.A., J.C. Wyngaard, Y. Izumi, E.F. Bradley, 1971: Flux-Profile Relationships in the Atmospheric Surface Layer. – J. Atmos. Sci., published online, DOI: 10.1175/1520-0469(1971)028<0181:Fprita>2.0.CO;2.

Carvalho, D., A. Rocha, C. Silva Santos, R. Pereira, 2013: Wind resource modelling in complex terrain using different mesoscale–microscale coupling techniques. – Appl. Energy **108**, 493–504, DOI: 10.1016/j.apenergy.2013.03.074.

Castellani, F., C. Busillo, F. Calastrini, G. Gualtieri, G. Molina, L. Terzi, 2006: An hybrid approach for downscaling RAMS data for Wind Resource Assessment in Complex Terrains. – In: European Wind Energy Conference, 1–4.

Castro, F.A., C. Silva Santos, J.C. Lopes da Costa, 2015: One-way mesoscale-microscale coupling for the simulation of atmospheric flows over complex terrain. – Wind Energy **18**, 1251–1272, DOI: 10.1002/we.1758.

Chen, F., J. Dudhia, 2001: Coupling an Advanced Land Surface–Hydrology Model with the Penn State–NCAR MM5 Modeling System. Part II: Preliminary Model Validation. – Mon. Wea. Rev.**129**, 587–604, DOI: 10.1175/1520-0493(2001)129<0587:Caalsh>2.0.CO;2.

Csiszar, I., G. Gutman, 1999: Mapping global land surface albedo from NOAA AVHRR. – J. Geophys. Res. Atmos.**104**, 6215–6228, DOI: 10.1029/1998JD200090.

Duraisamy, V.J., 2014: Downscaling wind energy resource from mesocale to local scale by nesting and data assimilation with a CFD model. – PhD Thesis. University of Paris-Est.

Duraisamy, V.J., E. Dupont, B. Carissimo, 2014: Downscaling wind energy resource from mesoscale to microscale model and data assimilating field measurements. – J. Physics: Conference Series **555**, 012031, DOI: 10.1088/1742-6596/555/1/012031.

Dyer, A.J., 1974: A review of flux-profile relationships. – Bound.-Layer Meteor. **7**, 363–372, DOI: 10.1007/BF00240838.

Fitch, A.C., J.B. Olson, J.K. Lundquist, J. Dudhia, A.K. Gupta, J. Michalakes, I. Barstad, 2012: Local and Mesoscale Impacts of Wind Farms as Parameterized in a Mesoscale NWP Model. – Mon. Wea. Rev. **140**, 3017–3038, DOI: 10.1175/MWR-D-11-00352.1.

Folch, A., J. Barcons, T. Kozono, A. Costa, 2016: High-resolution modeling of atmospheric dispersion of dense gas using Twodee-2. 1: application to the 1986 Lake Nyos limnic eruption. (December). – Nat. Hazards Earth Syst. Sci. **17**, 861–879, DOI: 10.5194/nhess-2016-343.

Garratt, J.R., 1992: The atmospheric boundary layer. – Cambridge, UK: Cambridge University Press.

Gopalan, H., C. Gundling, K. Brown, B. Roget, J. Sitaraman, J.D. Mirocha, W.O. Miller, 2014: A coupled mesoscale-microscale framework for wind resource estimation and farm aerodynamics. – J. Wind Enginer. Indust. Aerodyn. **132**, 13–26, DOI: 10.1016/j.jweia.2014.06.001.

Gravdahl, A.R., 1998: Meso Scale Modeling with a Reynolds Averaged Navier-Stokes Solver Assessment of wind resources along the Norwegian coast. – In: 31st IEA Experts Meeting State of the Art on Wind Resource Estimation, 1–14. Risø, Denmark.

Gutman, G., A. Ignatov, 1998: The derivation of the green vegetation fraction from NOAA/Avhrr data for use in numerical weather prediction models. – Int. J. Remote Sens. **19**, 1533–1543, DOI: 10.1080/014311698215333.

Han, J., S.P. Arya, S. Shen, Y. Lin, 2000: An Estimation and Energy Atmospheric Theory of Turbulent Dissipation Boundary Kinetic Energy Rate Based on Layer Similarity. – NASA technical report. Hampton, Virginia.

Hines, K.M., D.H. Bromwich, 2008: Development and Testing of Polar Weather Research and Forecasting (WRF) Model. Part I: Greenland Ice Sheet Meteorology*. – Mon. Wea. Rev. **136**, 1971–1989, DOI: 10.1175/2007MWR2112.1.

Hristov, Y., G. Oxley, M. Žagar, 2014: Improvement of AEP Predictions Using Diurnal CFD Modelling with Site-Specific Stability Weightings Provided from Mesoscale Simulation. – J. Physics: Conference Series **524** (Torque), 012116, DOI: 10.1088/1742-6596/524/1/012116.

Iacono, M.J., J.S. Delamere, E.J. Mlawer, M.W. Shephard, S.A. Clough, W.D. Collins, 2008: Radiative forcing by long-lived greenhouse gases: Calculations with the AER radiative transfer models. – J. Geophys. Res. Atmos. **113**, 2–9, DOI: 10.1029/2008JD009944.

Janjić, Z.I., 1994: The Step-Mountain Eta Coordinate Model: Further Developments of the Convection, Viscous Sublayer, and Turbulence Closure Schemes. – Mon. Wea. Rev. **122**, 927–945, DOI: 10.1175/1520-0493(1994)122<0927:Tsmecm>2.0.CO;2.

Katic, I., J. Højstrup, N.O. Jensen, 1987: A Simple Model for Cluster Efficiency. – EWEC'86. Proceedings 407-410.

Kinbara, K., S. Iizuka, M. Kuroki, A. Kondo, 2010: Merging WRF and LES models for the analysis of a wind environment in an urban area. – In: The Fifth Symposium Computational Wind Engineering.

Koh, T., R. Fonseca, 2016: Subgrid-scale cloud-radiation feedback for the Betts-Miller-Janjić convection scheme. – Quart. J. Roy. Meteor. Soc. **142**, 989–1006, DOI: 10.1002/qj.2702.

Leblebici, E., I. Tuncer, 2015: Wind Power Estimations using OpenFoam Coupled with WRF. – In: 11th EAWE PhD Seminar on Wind Energy in Europe.

Leblebici, E., G. Ahmet, I. Tuncer, 2014: CFD Coupled with WRF for Wind Power Prediction. – In: 10th PhD Seminar on Wind Energy in Europe. Orléans.

Li, L., F. Hu, J. Jiang, X. Cheng, 2007: An application of the RAMS/Fluent system on the multi-scale numerical simulation of the urban surface layer -A preliminary study. – Adv. Atmos. Sci. **24**, 271–280, DOI: 10.1007/s00376-007-0271-y.

Li, L., L. Zhang, N. Zhang, F. Hu, Y. Jiang, C. Xuan, W. Jiang, 2010: Study on the Micro-scale simulation of wind field over complex terrain by RAMS / Fluent modeling system. – The Fifth International Symposium on Computational Wind Engineering (CWE2010) 2(5), 411–418, DOI: 10.3724/SP.J.1226.2010.00411.

Liu, Y., T. Warner, Y. Liu, C. Vincent, W. Wu, B. Mahoney, S. Swerdlin, K. Parks, J. Boehnert, 2011: Simultaneous nested modeling from the synoptic scale to the LES scale for wind energy applications. – J. Wind Engineer. Indust. Aerodyn. **99**, 308–319, DOI: 10.1016/j.jweia.2011.01.013.

Liu, Y.S., S.G. Miao, C.L. Zhang, G.X. Cui, Z.S. Zhang, 2012: Study on micro-atmospheric environment by coupling large eddy simulation with mesoscale model. – J. Wind Engineer. Indust. Aerodyn. **107**, 106–117, DOI: 10.1016/j.jweia.2012.03.033.

Lo, J.C., Z. Yang, R.A. Pielke, 2008: Assessment of three dynamical climate downscaling methods using the Weather Research and Forecasting (WRF) model. – J. Geophys. Res.**113**, D09112, DOI: 10.1029/2007JD009216.

Loveland, T.R., B.C. Reed, J.F. Brown, D.O. Ohlen, Z. Zhu, L. Yang, J.W. Merchant, 2000: Development of a global land cover characteristics database and IGBP DISCover from 1 km Avhrr data. – Int. J. Remote Sens. **21**, 1303–1330, DOI: 10.1080/014311600210191.

Lundquist, J.K., J.D. Mirocha, B. Kosović, 2008: Nesting large-eddy simulations within mesoscale simulations in WRF for wind energy applications. – In: AGU Fall Meeting Abstracts **6**.

Meissner, C., A.R. Gravdahl, B. Steensen, 2009: Including Thermal Effects in CFD Wind Flow Simulations. – J. Env. Sci. Int. **18**, 833–839, DOI: 10.5322/JES.2009.18.8.833.

Meissner, C., M. Mana, J. Gentle, C.G. Nunalee, 2015: Coupling of mesoscale and microscale models for wind resource assessment and wind power forecasting. – ????

Miao, Y., S. Liu, B. Chen, B. Zhang, S. Wang, S. Li, 2013: Simulating urban flow and dispersion in Beijing by coupling a CFD model with the WRF model. – Adv. Atmos. Sci. **30**, 1663–1678, DOI: 10.1007/s00376-013-2234-9.

Mirocha, J., G. Kirkil, 2010: Nested high-resolution mesoscale / large eddy simulations in WRF: challenges and opportunities. – In: The Fifth International Symposium on Computational Wind Engineering (CWE2010). Chapel Hill, North Carolina, USA.

Mirocha, J., G. Kirkil, E. Bou-Zeid, F.K. Chow, B. Kosović, 2013: Transition and Equilibration of Neutral Atmospheric Boundary Layer Flow in One-Way Nested Large-Eddy Simulations Using the Weather Research and Forecasting Model. – Mon. Wea. Rev. **141**, 918–940, DOI: 10.1175/MWR-D-11-00263.1.

Mirocha, J., B. Kosovic, G. Kirkil, 2014: Resolved Turbulence Characteristics in Large-Eddy Simulations Nested within Mesoscale Simulations Using the Weather Research and Forecasting Model. – Mon. Wea. Rev. **142**, 806–831, DOI: 10.1175/MWR-D-13-00064.1.

Moeng, C., J. Dudhia, J. Klemp, P. Sullivan, 2007: Examining Two-Way Grid Nesting for Large Eddy Simulation of the PBL Using the WRF Model. – Mon. Wea. Rev. **135**, 2295–2311, DOI: 10.1175/MWR3406.1.

Monin, A.S., A.M. Obukhov, 1954: Basic laws of turbulent mixing in the surface layer of the atmosphere. – Contrib. Geophys. Inst. Acad. Sci. USSR **24**, 163–187.

Muñoz-Esparza, D., B. Kosovic, J. Mirocha, J. van Beeck, 2014: Bridging the Transition from Mesoscale to Microscale Turbulence in Numerical Weather Prediction Models. – Bound.-Layer Meteor. **153**, 409–440, DOI: 10.1007/s10546-014-9956-9.

Murakami, S., A. Mochida, S. Kato, 2003: Development of local area wind prediction system for selecting suitable site for windmill. – J. Wind Engineer. Indust. Aerodyn. **91**, 1759–1776, DOI: 10.1016/j.jweia.2003.09.040.

Nakanishi, M., H. Niino, 2004: An improved Mellor-Yamada Level-3 model with condensation physics: Its design and verification. – Bound.-Layer Meteor. 112, 1–31, DOI: 10.1023/B:BOUN.0000020164.04146.98.

Nakanishi, M., H. Niino, 2006: An improved Mellor-Yamada Level-3 model: Its numerical stability and application to a regional prediction of advection fog. – Bound Layer Meteor. **119**, 397–407, DOI: 10.1007/s10546-005-9030-8.

Nakayama, H., T. Takemi, H. Nagai, 2011: Coupling of WRF and building-resolving urban CFD models for analysis of strong winds over an urban area. – In: 14th Conference on Mesoscale Processes.

Nozu, T., T. Kishida, T. Tamura, Y. Okuda, H. Umakawa, 2009: LES of wind turbulence and heat environment around dense tall buildings. – In: Eacwe **5**, 1–10, Florence, Italy.

Saha, S., S. Moorthi, H. Pan, X. Wu, J. Wang, S. Nadiga, P. Tripp, R. Kistler, J. Woollen, D. Behringer, H. Liu, D. Stokes, R. Grumbine, G. Gayno, J. Wang, Y. Hou, H. Chuang, H. Juang, J. Sela, M. Iredell, R. Treadon, D. Kleist, P. Van Delst, D. Keyser, J. Derber, M. Ek, J. Meng, H. Wei, R. Yang, S. Lord, H. Van Den Dool, A. Kumar, W. Wang, C. Long, M. Chelliah, Y. Xue, B. Huang, J. Schemm, W. Ebisuzaki, R. Lin, P. Xie, M. Chen, S. Zhou, W. Higgins, C. Zou, Q. Liu, Y. Chen, Y. Han, L. Cucurull, R.W. Reynolds, G. Rutledge, M. Goldberg, 2010: The NCEP Climate Forecast System Reanalysis. – Bull. Amer. Meteor. Soc. **91**, 1015–1058, DOI: 10.1175/2010BAMS3001.1.

Sanz Rodrigo, J., B. García, D. Cabezón, S. Lozano, I. Martí, 2010: Downscaling mesoscale simulations with CFD for high resolution regional wind mapping. – In: European Wind Energy Conference EWEC-2010, Warsaw.

Sanz Rodrigo, J., R.A. Chávez Arroyo, P. Moriarty, M. Churchfield, B. Kosović, P.E. Réthoré, K. Hansen, A. Hahmann, J. Mirocha, D. Rife, 2017a: Mesoscale to microscale wind farm flow modeling and evaluation. – Wiley Interdisciplinary Revs. Energy Env. **6**, DOI: 10.1002/wene.214.

Sanz Rodrigo, J., M. Churchfield, B. Kosovic, 2017b: A methodology for the design and testing of atmospheric boundary layer models for wind energy applications. – Wind Energy Sci. **2**, 35–54, DOI: 10.5194/wes-2-35-2017.

Schneiderbauer, S., S. Pirker, 2010: Resolving unsteady micro-scale atmospheric flows by nesting a CFD simulation into wide range numerical weather prediction models. – Int. J. Comput. Fluid Dyn. **24**, 51–68, DOI: 10.1080/10618562.2010.483227.

Sitaraman, J., 2013: Simulation of Wind Turbine Performance and Loading Patterns using a Coupled Meso-scale/Micro-scale Flow Analysis Model. –Technical report, https://e-reports-ext.llnl.gov/pdf/765731.pdf

Sitaraman, J., H. Gopalan, C. Gundling, J. Mirocha, W. Miller, 2013: Coupled Mesoscale Microscale Model for Wind Resource Estimation and Turbine Aerodynamics Using an Overset Grid Approach. – In: 51st AIAA Aerospace Sciences Meeting including the New Horizons Forum and Aerospace Exposition, 1–23. Reston, Virigina: American Institute of Aeronautics and Astronautics, DOI: 10.2514/6.2013-1209.

Skamarock, W.C., J.B. Klemp, J. Dudhi, D.O. Gill, D.M. Barker, M.G. Duda, X. Huang, W. Wang, J.G. Powers, 2008: A Description of the Advanced Research WRF Version 3. – NCAR Technical Note NCAR/TN-468+STR, DOI: 10.5065/D6DZ069T.

Solazzo, E., A. Dudek, S. Oxizidis, R. Britter, T.E. Nordeng, 2006: From meso-scale to street-scale: a downscaling procedure using statistical and CFD models. The Lisbon case study. – In: 6th International Conference on Urban Climate. Göteborg.

Sutton, O.G., 1949: Atmospheric Turbulence. London, Methuen, 115 pp.

Takemi, T., T. Tamura, Y. Takei, Y. Okuda, 2006: Microscale analysis of severe winds within the urban canopy during a period of explosive cyclogenesis by coupling large-eddy simulation and mesoscale meteorological models. – In: The Fourth International Symposium on Computational Wind Engineering, 16–19, Yokohama.

Tao, W., J. Simpson, M. Mccumber, 1989: An Ice-Water Saturation Adjustment. – Mon. Wea. Rev., published online, DOI: 10.1175/1520-0493(1989)117<0231:Aiwsa>2.0.CO;2.

Tegen, I., P. Hollrig, M. Chin, I. Fung, D. Jacob, J. Penner, 1997: Contribution of different aerosol species to the global aerosol extinction optical thickness: Estimates from model results. – J. Geophys. Res. Atmos. **102**, D20, 23895–23915, DOI: 10.1029/97JD01864.

Veiga Rodrigues, C., J.M.L.M. Palma, 2014: Estimation of turbulence intensity and shear factor for diurnal and nocturnal periods with an Urans flow solver coupled with WRF. – J. Physics: Conference Series **524**, 012115, DOI: 10.1088/1742-6596/524/1/012115.

Veiga Rodrigues, C, M. Silva Santos, J.M.L.M. Palma, F.A. Castro, P.M.A. Miranda, A.H. Rodrigues, 2008: Short-term Forecasting of a Wind Farm Output using CFD. – In: European Wind Energy Conference and Exhibition 2008, Brussels.

Veiga Rodrigues, C., J.M.L.M. Palma, Á.H. Rodrigues, 2016: Atmospheric Flow over a Mountainous Region by a One-Way Coupled Approach Based on Reynolds-Averaged Turbulence Modelling. – Bound.-Layer Meteor. **159**, 407–437, DOI: 10.1007/s10546-015-0116-7.

Wang, J., R.M. Fonseca, K. Rutledge, J. Martín-Torres, J. Yu, 2019: Weather Simulation Uncertainty Estimation Using Bayesian Hierarchical Models. – J. Appl. Meteor. Climatol. **58**, 585–603, DOI: 10.1175/JAMC-D-18-0018.1.

Wharton, S., J.K. Lundquist, 2012: Assessing atmospheric stability and its impacts on rotor-disk wind characteristics at an onshore wind farm. – Wind Energy **15**, 525–546, DOI: 10.1002/we.483.

Yamaguchi, A., T. Ishihara, Y. Fujino, 2002: Applicability of Linear and Nonlinear Winnd Prediction Models To Wind Flow in Complex Terrain. – In: The World Wind Energy Conference and Exhibition, Berlin.

Yu, W., R. Benoit, C. Girard, A. Glazer, D. Lemarquis, J.R. Salmon, J.-P. Pinard, 2006: Wind Energy Simulation Toolkit (WEST): A Wind Mapping System for Use by the WindEnergy Industry. Wind Engineer. **30**, published online, DOI: 10.1260/030952406777641450.

Zheng, Y., Y. Miao, S. Liu, B. Chen, H. Zheng, S. Wang, 2015: Simulating flow and dispersion by using WRF-CFD coupled model in a built-up area of Shenyang, China. – Adv. Meteor. 2015, 528618, DOI: 10.1155/2015/528618.